

The Hebrew University of Jerusalem
Faculty of Mathematics and Sciences
Selim and Rachel Benin School of Engineering
Applied Physics Department



Photonic Analog-to-Digital Conversion Using Spatial Oversampling

המרה פוטונית של אות אנלוגי לדיגיטלי בעזרת
דגימת-יתר מרחבית

by

Ori Golani

This work was done under the supervision of

Prof. Dan M. Marom

Thesis submitted for M.Sc. degree

December, 2013

Abstract

Photonic analog to digital converters (ADC) have been the focus of much research interest in recent years, because of their potential for very high bandwidth and sampling rates. Using photonic techniques may help to surpass the limitations of traditional electronic analog to digital converters, providing unprecedented performance. A key parameter of any ADC is its conversion resolution. This work explores the technique of spatial oversampling as a means to increase resolution in photonic ADCs. Spatial oversampling is shown to be equivalent to temporal oversampling, a commonly used technique in the field of digital signal processing. The properties, benefits and requirements of spatial oversampling are derived, and the concept is demonstrated theoretically and experimentally. A photonic ADC design based on this technique is described, and an implementation as a photonic integrated circuit is presented. The design is based on electro-optic phase modulation, interferometric detection and spatial oversampling. The abilities and performance of this photonic ADC concept are demonstrated experimentally by digitizing analog signals with frequencies of up to 13GHz.

תקציר

ממירי אות אנלוגי לדיגיטלי המבוססים על פוטוניקה היוו נושא למספר רב של מחקרים בשנים האחרונות. זאת בגלל יכולתם לספק רוחב סרט וקצב דגימה גבוהים מאוד. שימוש בטכניקות פוטוניות יכול לעקוף את המגבלות של ממירים אלקטרוניים הנפוצים כיום, ולספק ביצועים חסרי תקדים. תכונה חשובה של ממיר אנלוגי לדיגיטלי הינה רזולוציית ההמרה, המבטאת את דיוק המערכת. עבודה זו בוחנת את הטכניקה של דגימת-יתר מרחבית כאמצעי לשיפור הרזולוציה של ממירים פוטוניים. נראה כי דגימת-יתר מרחבית הינה שקולה לדגימת-יתר זמנית-טכניקה נפוצה בתחום של עיבוד אותות דיגיטלי. תכונותיה והדרישות של טכניקת דגימת-יתר המרחבית מוצגות, ויכולתיה מודגמות בצורה תיאורתית וניסיונית. בהתבסס על טכניקה זו, אתאר ממיר פוטוני של אות אנלוגי לדיגיטלי, ואציג את מימושו כמעגל פוטוני משולב. הממיר מבוסס על אפנון פאזה אלקטרו-אופטי, גילוי אינטרפרומטרי ודגימת יתר מרחבית. יכולותיו ורמת הביצועים של הממיר הפוטוני מודגמות באופן ניסיוני ע"י המרה דיגיטלית של מספר אותות אנלוגיים, בתדירויות של עד 13 גיגה-הרץ.

Contents

1. Introduction	2
2. Theoretical Background	3
2.1. Overview of electronic ADCs	3
2.2. Overview of photonic ADCs	5
2.3. Electro-optic sampling	7
2.4. Optical hybrids	10
2.5. Spatial oversampling	12
3. System design	15
3.1. Star-coupler based optical hybrids	15
3.2. WDM pulse stream generation	18
3.3. Detection, digitization and DSP	20
3.4. Noise analysis	22
4. Experimental results	25
4.1. WDM pulse stream generation	25
4.2. Star-coupler fabrication and characterization	25
4.3. Spatial oversampling without optical sampling	26
4.4. Phase modulator and star-coupler integration	27
4.5. Experimental setup	29
4.6. PADC results	31
6. References	35
Appendix A- Measured coupling parameters of integrated star-couplers	39
Appendix B- Digital corrections for errors introduced by experimental setup	40

1. Introduction

Analog-to-digital converters (ADC) are a key component in many modern technologies. Present wherever the digital world interfaces with the analog world, ADCs have found uses across many fields and applications. Some examples of these are radio communication, test & measurement systems, digital control systems, electronic warfare and many more. The ever-growing speed and efficiency of integrated electronic circuits have pushed the speed and resolution of modern ADCs to unprecedented levels. However, the progress of ADCs is slower than semiconductor technology evolution, falling short of Moore's law [1]. Most single-block ADCs operate at sampling rates lower than 1GS/s- not fast enough for many applications. In order to overcome this limit, many ADCs rely on parallelism, using time interleaving of multiple sub-ADCs [2]. This technique can provide high sampling rates, at a cost of increasing the complexity of the ADC system. Careful calibration of the multiple sub-ADCs is needed to ensure a good sampling of the analog signal [3]. A key part of an ADC is the front-end sample-and-hold (S/H) circuit. This is an analog circuit whose function is to sample the input signal and hold it steady for the ADC to quantize it. An implication of time-interleaving is that the requirement of the S/H are higher. In high speed ADCs the S/H circuit is often the limiting factor, determining the bandwidth and resolution of the whole system [4].

Photonic analog-to-digital converters (PADC) are ADCs where some or all of the conversion process takes place in the optical domain. These are devices whose input is an analog electrical signal and output is a digital bit stream, and whose inner workings are based on optical processing. Optics offer many advantages over electronics; a practically unlimited bandwidth (many Terahertz, compared to a few Gigahertz in electronics), low timing jitter of optical pulses and relatively easy to achieve parallel operation through the use of wavelength division multiplexing (WDM). For these reasons, PADCs have been extensively researched in past years [5].

The object of this work is to explore a specific implementation of a PADC- A photonic analog-to-digital converter based on electro-optic phase modulation and spatial oversampling. Section 2 of this work provides a review of previously designed PADCs, detailed explanations on the principles of operation of the suggested PADC, and an analysis of the sub-systems that compose it. Section 3 provides details on our implementation of the PADC, fabrication of its components, and analysis of its performance. Section 4 provides experimental results and characterization of system performance. Section 5 concludes this work and discusses future direction of research.

2. Theoretical Background

2.1. Overview of electronic ADCs

Sampling is the process of converting a continuous-time signal to discrete-time signal, typically with equally spaced sample times. Quantization is the process of converting a continuous-voltage (or any other physical quantity) into a discrete number of values, called quantization levels. The function of an ADC is to sample and digitize a continuous signal. Three main factors determine the performance of an ADC: electrical bandwidth, sampling rate and resolution. For an ideal (noiseless) ADC, resolution is determined by the number of quantization levels, measured in bits. However, in most cases the digitization process suffer from noise. In these cases the ADC's resolution is measured in effective number of bits (ENOB) - a quantity taking into account noise and distortion introduced by the ADC. The effective number of quantization levels is defined as the signal's dynamic range, divided by the noise standard deviation. The relationship between ENOB and signal to noise ratio of the digitized signal can therefore be expressed as [1]:

$$ENOB = \frac{SNR - 1.76}{6.02} \quad (2.1.1)$$

Where the SNR is expressed in dB. In many ADC implementations, the digitization process requires multiple operations, both in the analog and digital domain [6]. For accurate digitization to take place, the input voltage must be held steady for a certain amount of time ("hold time"). This is the function of the S/H circuit [7]. A common method used to obtain a higher sampling rate than that defined by the hold time is time-interleaving. In this architecture, the signal is divided across many sub-ADCs, each one responsible to digitize a different time fragment. Time-interleaving requires an electronic front-end, dividing the signal to each sub-ADC and

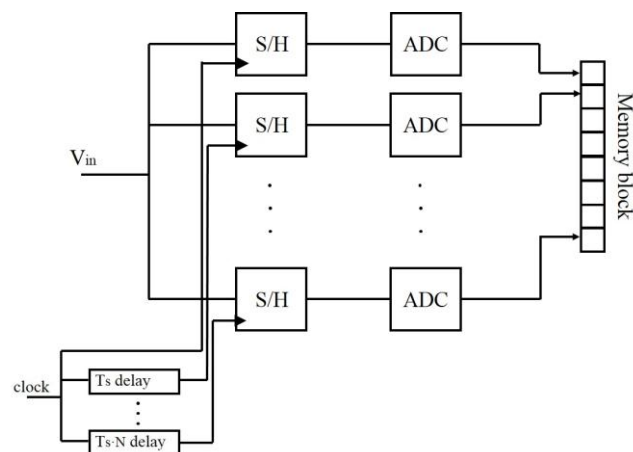


Fig. 1- Schematic layout of a time-interleaved ADC

synchronizing their operation. Figure 1 shows a schematic layout of a time-interleaved ADC. For a target sampling rate of f_s and an interleaving factor of N , the required sampling rate of each ADC is only f_s/N . It is important to note that the ADC's overall bandwidth is determined by the S/H circuit. Using time interleaving does not alleviate the requirements of the S/H, leaving it as the limiting factor on the ADC's performance. Errors in each S/H timing, gain and DC offsets can severely degrade the performance of a time-interleaved ADC [3].

An important source for digitization errors is timing jitter. Variations the clock's frequency cause the S/H to sample the signal at the wrong time, amounting to random noise [8]. Let the sampling time of the n 'th sample point be:

$$\begin{aligned} T_n &= T_s \cdot n + \tau \\ \tau &\sim N(0, \Delta\tau) \end{aligned} \quad (2.1.2)$$

Where $\Delta\tau$ is the clock's timing jitter, which is determined on the microelectronic technology used. The magnitude of this noise is determined on the signal's frequency. Assuming the ADC operates at the Nyquist frequency ($f_s/2$) and covering the full ADC dynamic range, the limits on ADC resolution is:

$$ENOB \leq -\log_2 \left(\sqrt{3\pi} f_s \Delta\tau \right) \quad (2.1.3)$$

Equation 2.1.3 shows a fundamental trade-off: given certain timing jitter, increasing the sampling rate and bandwidth reduces the maximal resolution. Timing jitter in state-of-the-art electronics is on order of 100fs, making it the limiting factor in high speed ADCs.

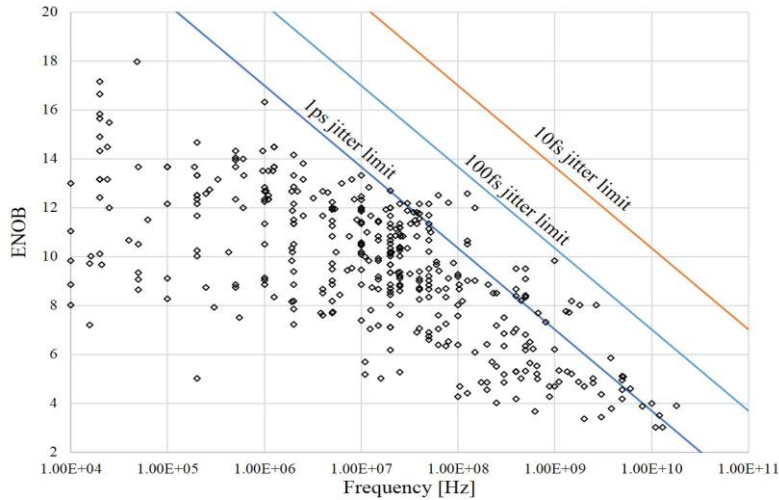


Fig. 2- A survey of state-of-the-art electronic ADCs, performed by [9]. Black markers represent the ENOB and bandwidth of ADCs reported in literature. Straight lines show the theoretical limit imposed by timing jitter.

2.2. Overview of photonic ADCs

Photonic ADCs has been suggested as early as the 1970's [10], but have not yet been used in commercial devices. Generally, a PADC will use an electro-optic modulator to encode an electrical input on an optical carrier signal. This signal will then be manipulated in the optical domain. PADCs may categorized to several groups, based on two main function of an ADC- sampling and quantization [5].

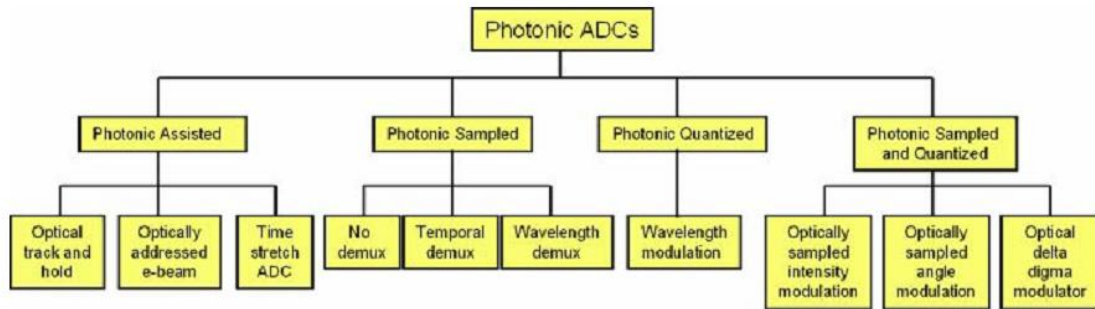


Fig.3- groups of photonic ADCs, as defined in [5]

Most photonic-assisted PADCs use an optical pulse stream to sample the electric signal, as will be discussed thoroughly in section 3.1. Quantization is the process of converting a continuous voltage signal into discrete levels- namely converting the continuous input signal into bits. Quantization can take place either in the electrical or the optical domain, the latter typically using either non-linear optics or a cascade of optical modulators. Photonic-assisted sampled (but not quantized) PADCs use an electrical ADC to quantize the signal after detection. A notable example of photonic-assisted sampled PADCs is the recent work done by Kärtner et al., who used pulses from mode-locked laser and an electro-optic amplitude modulator to sample an electrical signal [11, 12]. This type of implementation is approaching practical on-chip implementation on a silicon-photonics platform [13, 14]. A similar concept, using an electro-optic phase modulator, was demonstrated by Kanter et al. [15].

Photonic-assisted sampled and quantized PADCs typically employ some method of optical coding- where the input RF signal shifts the optical signal either in the spectral or the spatial domain. The coded signal is then directly detected using simple photodiodes (i.e. without electronic ADC), digitizing the signal in the optical domain. Quantization through spectral encoding can be achieved by using a cascade of modulators [16], or by using non-linear optics. This has been demonstrated by Itoh et al. using soliton self-frequency shift in a non-linear medium [17-19]. In this implementation soliton pulses are passed through an electro-optic modulator to achieve sampling, and through a non-linear fiber to be quantized using self-

frequency shift and optical coding. Spatial optical coding has been demonstrated by using phase modulation and free space interference, creating an optical equivalent to a flash ADC [20-22]. A completely different approach to photonic quantization was offered by Nazarathy [23], creating optical analogues to electronic building blocks commonly used in ADCs.

Photonic-assisted ADCs (PAADC) take a completely different route. In these implementations, both the sampling and quantization take place in the electronic domain. Photonics are used to facilitate the process and increase conversion rate. An interesting example is that of time-stretched PAADCs, pioneered by Jallali et al. [24, 25]. A chirped optical signal is modulated by the electrical signal, and passed through a highly dispersive medium. The dispersion “stretches” the chirped signal, effectively slowing it down. Detection and digitization using slow electronics then takes place, providing sampling of fast signals using slow electronics, albeit of a finite duration unless WDM de-multiplexing concepts are introduced.

Another concept commonly used in PADCs, most notably in photonic-sampled PADCs, is rate multiplication using wavelength division multiplexing (WDM). In this approach, the sampling optical signal is a series of pulses, each with a different wavelength. After the sampling process, the pulses are separated using a de-multiplexer and quantized using slower electronics working in parallel [26]. This technique is essentially equivalent to time interleaving in electronic ADCs, where the part of the sample and hold circuit is replaced by optics. It has, however, some key advantages over its electrical counterpart- The WDM splitting does not incur much added losses; the process can be done using passive optics, thus not adding any new jitter sources; The method does not impose new limitation on the electronics, as the bandwidth needed remains low. Like time interleaved ADCs, the sub-ADCs in a WDM-PADC can work in a fraction of the overall sampling rate, according to the number of WDM channels employed.

The PADC presented in this work is of the photonic sampled, electronically quantized group. It uses a WDM pulse stream and an electro-optic phase modulator for optical sampling,

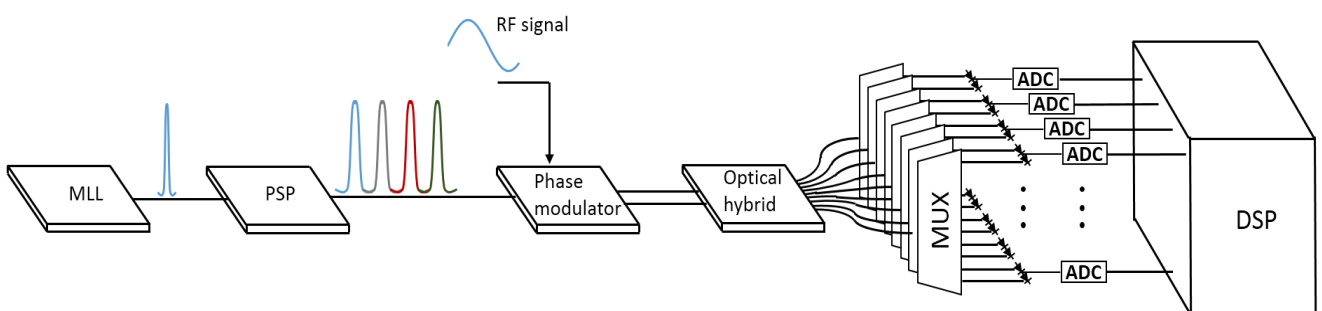


Fig. 4- Block level description of proposed PADC

and coherent detection followed by signal processing for quantization. Figure 4 shows a block-level description of the proposed system. The PADC uses a mode-locked laser (MLL), combined with a photonic spectral processor (PSP), as a source of sampling WDM pulses. Coherent detection then takes place using a fine optical hybrid. The advantages of fine optical hybrids, compared to standard 90° optical hybrid and non-coherent detection, are discussed in section 2.5. Using a series of WDM de-multiplexers, the sampled signal is split and detected using low-speed electronics. Thus, time interleaving is achieved. This design is essentially a combination of a photonic-sampled electronically-quantized PADC and an interferometric PADC, combining the favorable attributes of both types.

2.3. Electro-optic sampling

We turn now to analyze the process of sampling a continuous signal with a pulse stream. For simplicity, we consider first the case of amplitude modulated pulses without time interleaving. A common mathematical treatment of ideal sampling is considering the sampling process as a multiplication of the signal and an impulse train [27]. Namely:

$$x_{samp}(t) = x(t) \cdot \left(\sum_{-\infty}^{\infty} \delta(t - nT_s) \right) = \begin{cases} x(nT_s), & t = nT_s, n \in \mathbb{Z} \\ 0, & \text{else} \end{cases} \quad (2.3.1)$$

Where $x(t)$ is the signal to be sampled, x_{samp} the ideal sampled signal, T_s the sampling time and δ the Dirac delta function. Naturally, a delta function cannot be created in physical reality. Instead, let us consider short pulses as a sampling signal. Replacing the delta function with pulses of width τ and the convolution with multiplication we get:

$$x_{samp}(t) = x(t) \cdot \left(\sum_{-\infty}^{\infty} P(t - nT_s) \right) \cong \begin{cases} x(nT_s), & nT - \frac{\tau}{2} < t < nT + \frac{\tau}{2}, n \in \mathbb{Z} \\ 0, & \text{else} \end{cases} \quad (2.3.2)$$

Where $P(t)$ is the pulse shape. Here it is assumed that the signal does not vary during a pulse width, and that the pulse train has no energy outside of the pulses. The effects of pulse shape and the change in signal level during a pulse width are analyzed later. The sampling process is complete using finite time integration, converting the continuous signal into discrete one:

$$x[n] = \int_{nT_s - \tau/2}^{nT_s + \tau/2} x_{samp}(t) dt = x(nT_s) \quad (2.3.3)$$

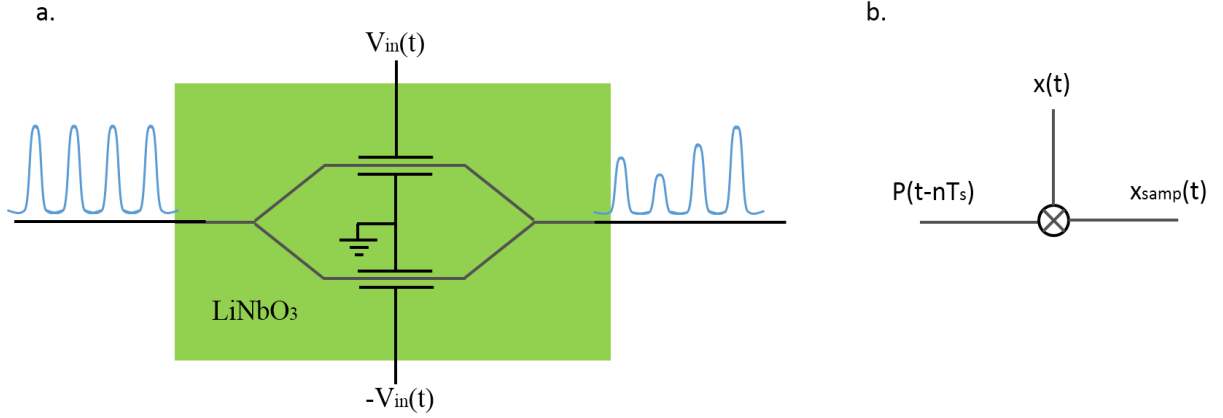


Fig. 5- a. Illustration of electro-optic sampling using a LiNbO₃ modulator. b. Block diagram representation of the process

In a physical system, this finite time integration is done using an Integrate-and-Hold circuit (I/H) [28]. The bandwidth requirements of such a circuit are smaller than that of a sample and hold circuit, making it feasible for high speed systems.

An easy way to implement the sampling process is using an electro-optic modulator, such as a LiNbO₃ modulator. This device encodes an electrical information in the optical domain.

Returning to analyze the effects of pulse shape on the sampling process, we express sampling with an optical pulse stream as:

$$x_{samp}(t) = x(t) \cdot \sum_{-\infty}^{\infty} P(t - nT_s) \quad (2.3.4)$$

Where $x(t)$ the signal to be sampled, x_{samp} the sampled signal, and $P(t)$ the sampling pulse shape. This may be expressed as:

$$x_{samp}(t) = \left(x(t) \cdot \left(\sum_{-\infty}^{\infty} \delta(t - nT_s) \right) \right) \otimes P(t) \quad (2.3.5)$$

$$x_{samp}(t) = x_{ideal}(t) \otimes P(t)$$

Where x_{ideal} is the ideally-sampled signal, i.e. sampling with a delta-function series. Taking the pulses as Gaussian with width τ , and looking at the spectrum of the sampled signal, we get:

$$P(t) = e^{-\left(\frac{t}{2\tau}\right)^2} \quad (2.3.6)$$

$$X_{samp}(f) = X_{ideal} \cdot \frac{\sqrt{\pi}}{2\tau} e^{-(2\pi\tau f)^2}$$

Thus, we conclude that the finite pulse width and shape act as a Gaussian low-pass filter on the signal. This limits the frequency range of the input signal, and the -3dB cutoff frequency is given by:

$$f_{cutoff} = \frac{\ln 2}{4\pi} \cdot \frac{1}{\tau} \quad (2.3.7)$$

A significant drawback of using electro-optic amplitude modulators is the linearity limit of the device. The output power-voltage response of a standard Mach-Zehnder interferometer (MZI) based modulator is given by [29]:

$$P = P_{in} \cdot \cos^2 \left(\frac{\pi V}{V_{\pi}} \right) \quad (2.3.8)$$

When a bias voltage of $V_{\pi}/4$ is applied, the response is approximately linear.

$$P \cong P_{in} \cdot \left(\frac{1}{2} + \frac{\pi V}{V_{\pi}} + O(V^2) \right) \quad (2.3.9)$$

Under the conditions of linearity, an MZI behaves as required by equation (2.3.2) (the $\frac{1}{2}$ term may be easily removed using a DC block filter). However, the high order terms become significant when a higher voltage is applied. This can be handled either by removing the non-linearity with additional circuitry (analog or digital), or by limiting the input voltage range. In all cases, the non-linearity reduces the dynamic range of quantization and adds to system complexity.

The case of electro-optic phase modulation follows similar principles. The input voltage signal is converted to phase-only modulation, $x(t)$ (with unity amplitude), namely:

$$x(t) = \exp \left(i \frac{\pi V}{V_{\pi}} \right) \quad (2.3.10)$$

This type of modulation can be easily achieved using an electro-optic phase modulator, and presents much better linearity than amplitude modulation. This method encodes the information in the optical phase domain. As optical phase cannot be directly measured, a PADC using phase modulation must also employ interference-based coherent detection. Figure 6 show a schematic layout of phase domain sampling scheme. The methods and devices needed for detecting phase information are discussed in section 3.1.

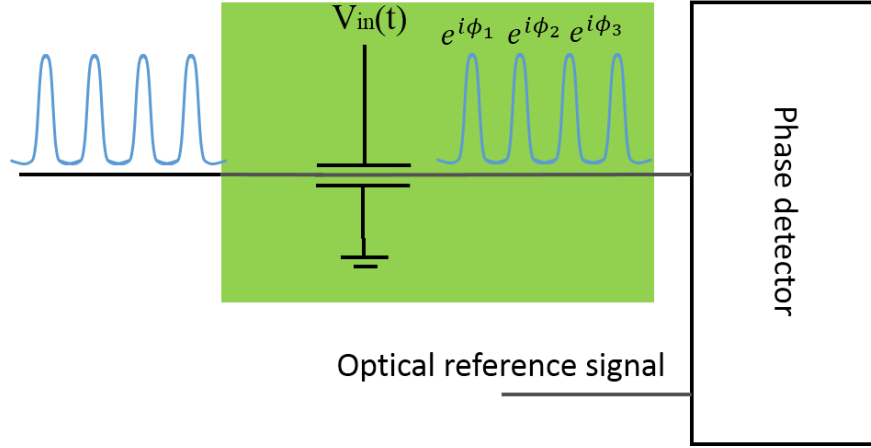


Fig. 6- Illustration of electro-optic sampling using a LiNbO₃ phase modulator.

2.4. Optical hybrids

Optical coherent detection is the detection of both the amplitude and phase of an optical signal. It is often based on the interference of the signal and a reference signal. The optical signal may be treated as a complex variable. The real and imaginary parts of the signal are denoted I and Q (In-phase and Quadrature), respectively. In the most general case, these terms are independent, and therefore at least two measurements are required for a full estimation of both the phase and amplitude. An optical hybrid is a device commonly used to mix signal and reference in coherent detection schemes. A $360^\circ/N$ optical hybrid is a 2-input- N -output device, whose outputs are linear combinations of the two inputs with different phase differences. The electrical field in the n 'th output of an optical hybrid is:

$$E_n = S + R \cdot e^{i\frac{2\pi n}{N}}, \quad n \in 0 \dots N-1 \quad (2.4.1)$$

Where S, R are the input signal and reference fields. The output optical power is therefore:

$$P_n = |E_n|^2 = |S|^2 + |R|^2 + 2|S \cdot R| \cdot \cos\left(\frac{2\pi n}{N} - \Delta\phi\right), \quad n \in 0 \dots N-1 \quad (2.4.2)$$

Where $\Delta\phi$ is the phase difference between the signal and reference. Assuming the reference is known, two measurements are sufficient to reconstruct the amplitude and phase of the signal. As the cosine is a periodic function, these two measurements must be 90° apart on the complex plane [30]. In order to remove the phase-independent terms of equation (2.3.8) (first two terms), many schemes employ balanced photodiodes as detectors. This doubles the number of required optical output ports (but not the electrical) and improves the dynamic range by 3dB. Each pair

of outputs that are 180° apart on the complex plane are fed to a balanced photodiode, providing the photocurrents:

$$I_n = \frac{4}{N} \Re\{S \cdot R\} \cdot \cos\left(\frac{2\pi}{N} - \Delta\phi\right), n \in 0 \dots \frac{N}{2} - 1 \quad (2.4.3)$$

Where \Re is the photodiode's responsivity. The most commonly used optical hybrid is the 90° optical hybrid- the minimal number of output ports required. This provides the real and imaginary parts of the signal directly:

$$\begin{pmatrix} I_0 \\ I_1 \end{pmatrix} = \begin{pmatrix} Q \\ I \end{pmatrix} = \Re\{S \cdot R\} \cdot \begin{pmatrix} \cos(\Delta\phi) \\ \sin(\Delta\phi) \end{pmatrix} \quad (2.4.4)$$

The I/Q measurements can be treated as projections of the signal on the main axes of the complex plane. A $360^\circ/N$ optical hybrid provides $N/4$ such projections, on multiple tilted axes. Each pair of measurement that are 90° apart may be considered separately as such a projection:

$$\begin{pmatrix} I_n \\ I_{n+N/4} \end{pmatrix} = \frac{4\Re\{S \cdot R\}}{N} \cdot \begin{pmatrix} \cos(\Delta\phi - 2\pi n/N) \\ \sin(\Delta\phi - 2\pi n/N) \end{pmatrix}, n \in 0 \dots \frac{N}{4} \quad (2.4.5)$$

While each of these pairs is sufficient to estimate the phase, using all of them is beneficial when noise is added to the process. The effects of noise are considered in section 2.4. The I/Q measurements may be estimated by taking the projections of each of these measurements on the main axes:

$$\begin{pmatrix} Q \\ I \end{pmatrix} = \frac{1}{2} \sum_{n=0}^{N/2-1} I_n \cdot \begin{pmatrix} \cos(2\pi n/N) \\ \sin(2\pi n/N) \end{pmatrix} \quad (2.4.6)$$

The PADC in this work use a self-coherent phase detection scheme. Self-coherent schemes are these where the signal is interfered with a copy of itself, and not an external source. These have the advantage of being immune to phase noises from the sampling pulses source, as the phase is common to both interfering paths. The optical source is split, prior to modulation, to two arms. One arm undergoes phase modulation, as described in figure 6, and the other is fed directly to the optical hybrid. Equation (2.4.3) then becomes:

$$I_n = \frac{4}{N} \Re \cdot P \cdot \cos\left(\frac{2\pi}{N} - \Delta\phi\right), n \in 0 \dots \frac{N}{2} - 1 \quad (2.4.7)$$

Where P is the total optical power passed to the system, minus excess losses.

We turn now to review some of the methods used to implement an optical hybrid. Several methods to realize optical hybrids have been proposed in past years. Classic designs for a 90° optical hybrid are based on waveguide directional couplers [31]. Each of the inputs are split to

N different paths, each path with a different length, providing the needed phase offsets. Connecting paths originating from the two inputs provides the needed outputs. This method does not easily scale to finer optical hybrids, as the number of couplers and waveguide crossings required increases with the number of ports.

A more suitable approach for multi-port optical hybrids is using multi-mode interference (MMI) devices. These devices use imaging of the input ports on a series of output ports [32-34]. In order to achieve the needed phase relations, more than one MMI segment is needed in the device. Star couplers can also be used as 90° hybrids [35] and are easily scalable. These are based on Fourier optics, as the star coupler's curved output plane is a Fourier transform of the curved input plane [36]. The optical hybrids used for implementing the PADC in this work are based on star couplers. They are discussed in detail in section 3.1.

2.5. Spatial oversampling

While electro-optic sampling determines the system's bandwidth and provides low jitter characteristics, resolution will be determined by the electronic detection and ADCs. Even when utilizing time interleaving by WDM parallelism, an overall sampling rate of tens of gigahertz will require each sub-ADC to work at several gigahertz. At these rates ADCs often suffer from a low resolution. One goal of this work is to demonstrate that a photonic ADC resolution can be greatly improved by using an additional level of parallelism- A multi-point instantaneous measurement of the modulated signal can be used in conjunction with digital signal processing (DSP) to provide better signal estimation.

As described in the previous section, two interference measurements are sufficient for a full estimation of the optical phase. Taking more measurements than needed is termed "oversampling", and if these measurements occur at different spatial points "spatial oversampling". In the field of DSP, oversampling usually refers to sampling faster than the Nyquist rate (temporal oversampling). An important reason for temporal oversampling is to improve resolution [37]. It has been shown that for an ADC with a resolution of B bits, using temporal oversampling by a factor of M , it is possible to achieve an effective resolution of:

$$B_{\text{effective}} = B + \frac{1}{2} \cdot \log_2 M \quad (2.5.1)$$

However, this increase in resolution comes at a severe reduction in the available bandwidth- for a sampling rate of f_s , the maximal bandwidth is $f_s/(2N)$. For high-speed ADCs this tradeoff is not acceptable. The concept of spatial oversampling use the same principles as temporal oversampling, but trading the bandwidth reduction into an increase in hardware. In order to

achieve an oversampling factor of N , multiple instantaneous measurements will be taken using N parallel sub-ADCs. However, one cannot simply divide the signal to several detectors and expect a noise improvement, because the divided signals will be strongly correlated- For spatial oversampling to work, the sub-ADC's noise terms must be independent. Using an optical hybrid means that all of the photocurrent measurements will be divided across the sub-ADCs full dynamic range, ensuring that their quantization noise factors will be independent. In order to understand the oversampling process, we look at the output photocurrents of an optical hybrid, as described in equation (2.4.3), corrupted by noise.

$$I_n = \frac{4}{N} \Re |S \cdot R| \cdot \cos\left(\frac{2\pi}{N} - \Delta\phi\right) + i_n, n \in 1 \dots \frac{N}{2} \quad (2.5.2)$$

$$i_n \sim N(0, \sigma)$$

The noise term i_n is taken a Gaussian noise with zero mean a variance of σ^2 , and is independent for each detector. The signal-to-noise ratio (SNR) of each measurement, assuming an equal distribution of phase, is:

$$SNR_n = \frac{1}{2} \left(\frac{4\Re |S \cdot R|}{N} \right)^2 / \sigma^2 \quad (2.5.3)$$

Plugging equation (2.5.3) in equation (2.4.6) gives the noisy I/Q measurements:

$$Q = \frac{1}{2} \sum_{n=0}^{N/2-1} \left(\frac{4}{N} \Re |S \cdot R| \cdot \cos\left(\frac{2\pi}{N} - \Delta\phi\right) + i_n \right) \cdot \cos(2\pi n/N) =$$

$$= \Re |S \cdot R| \cdot \cos(\Delta\phi) + \sum_{n=0}^{N/2-1} (i_n \cdot \cos(2\pi n/N)) \quad (2.5.4)$$

$$I = \frac{1}{2} \sum_{n=0}^{N/2-1} \left(\frac{4}{N} \Re |S \cdot R| \cdot \cos\left(\frac{2\pi}{N} - \Delta\phi\right) + i_n \right) \cdot \sin(2\pi n/N) =$$

$$= \Re |S \cdot R| \cdot \sin(\Delta\phi) + \sum_{n=0}^{N/2-1} (i_n \cdot \sin(2\pi n/N))$$

Denoting i_i, i_Q the noise terms of the I/Q terms respectively, and remembering that all individual noise terms are independent:

$$\text{var}(i_Q) = \text{var}\left(\sum_{n=0}^{N/2-1} (i_n \cdot \cos(2\pi n/N))\right) = \sum_{n=0}^{N/2-1} (\cos^2(2\pi n/N) \cdot \text{var}(i_n)) = \frac{N}{4} \sigma^2 \quad (2.5.5)$$

$$\text{var}(i_I) = \text{var}\left(\sum_{n=0}^{N/2-1} (i_n \cdot \sin(2\pi n/N))\right) = \sum_{n=0}^{N/2-1} (\sin^2(2\pi n/N) \cdot \text{var}(i_n)) = \frac{N}{4} \sigma^2$$

And the I/Q SNR:

$$SNR_Q = SNR_I = \frac{1}{2} \left(4\Re\{S \cdot R\} \right)^2 / \left(\frac{4\sigma^2}{N} \right) = \frac{N}{4} \cdot SNR_n \quad (2.5.6)$$

Where SNR_n is the signal-to-noise ratio of a single detector. As we use phase encoding, the more important quantity is the variance of the phase measurement. Given the I/Q measurements and variances, the phase variance may be found using the chain rule:

$$\Delta\phi = \frac{\partial\phi}{\partial I} \Delta I + \frac{\partial\phi}{\partial Q} \Delta Q = \frac{Q \cdot \Delta I - I \cdot \Delta Q}{I^2 + Q^2} \quad (2.5.7)$$

Working in a normalized complex space ($I^2 + Q^2 = 1$), and using that the I/Q variances are equal, we get:

$$\text{var}(\Delta\phi) = Q^2 \cdot \text{var}(\Delta I) + I^2 \cdot \text{var}(\Delta Q) = \text{var}(\Delta Q) = \text{var}(\Delta I) \quad (2.5.8)$$

The normalized I/Q measures are in the $[-1, 1]$ range and the phase in the $[0, 2\pi]$ range, and thus the phase SNR may be expressed as:

$$SNR_\phi = \pi^2 \cdot SNR_{I,Q} = \frac{\pi^2 N}{4} \cdot SNR_n \quad (2.5.9)$$

Converting this into ENOB using equation 2.1.1, and assuming each detector has an effective resolution of B , equation (2.5.9) becomes:

$$ENOB = B + \log_2 \pi + \frac{1}{2} \log_2 \left(\frac{N}{4} \right) \quad (2.5.10)$$

Defining the oversampling factor $M=N/4$ (as four output ports is the minimal required number), this result is almost identical to that of temporal oversampling, shown in equation (2.5.1). The $\log_2 \pi$ terms results from the dynamic range increase of using phase modulation. This analysis holds for every type of noise, but assumes that increasing N does not change the SNR of each detector. In a practical implementation, increasing the parallelism also decrease the power at each point and may affect the SNR. This effect, as well as the specific noise sources that limit the resolution are considered in section 3.3.

3. System design

3.1. Star-coupler based optical hybrids

The optical hybrids described in section 2.4 can be implemented in the form of a star coupler. The key part of a star coupler is a confocal slab lens, shown in figure 7. As in all slab waveguide structures, an electrical field passed through the lens can be treated as confined in the y axis, and freely propagating in the remaining two axes.

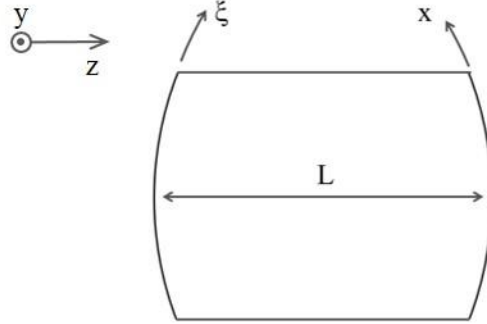


Fig. 7- Geometry of a confocal slab lens

Denoting spatial coordinates of the left and right curved plane ξ and x , respectively. For a curve radius L for the two planes, the distance between two points on the planes may be approximated as:

$$D(\xi, x) \cong L - \frac{x\xi}{L} \quad (3.1.1)$$

Here the paraxial approximation was used, expanding the distance to the first order Taylor series. Assuming some electric field distribution on the left plane, $E(\xi)$, and an effective refractive index n_0 in the slab waveguide, the diffraction pattern on the right plane is:

$$E(x) = \int E(\xi) \cdot e^{i \frac{2\pi n_0}{\lambda} D(\xi, x)} d\xi = e^{i \frac{2\pi n_0}{\lambda} L} \cdot \int E(\xi) \cdot e^{-i \frac{2\pi n_0}{\lambda} \frac{\xi x}{L}} d\xi \quad (3.1.2)$$

Thus the field at the right plane is a Fourier transform of the left plane. Placing two input waveguides symmetrically about the optical axis of the slab lens, separated by distance d and perpendicular to the input (left) plane, gives the input field:

$$E(\xi) = S \cdot \exp\left(-\frac{(\xi - d/2)^2}{\Delta^2}\right) + R \cdot \exp\left(-\frac{(\xi + d/2)^2}{\Delta^2}\right) \quad (3.1.3)$$

Where Δ is the waveguide mode width (assumed to be Gaussian), S and R are the input fields of each waveguide. The diffraction pattern at the output (right) plane is:

$$E(x) = \left(S \cdot e^{-\pi i \frac{n_0 d}{\lambda L} x} + R \cdot e^{\pi i \frac{n_0 d}{\lambda L} x} \right) \cdot \sqrt{\pi \Delta^2} e^{-\left(\pi \frac{n_0 \Delta}{\lambda L} x \right)^2} \quad (3.1.4)$$

And thus the power distribution:

$$P(x) \propto \left(|R|^2 + |S|^2 + 2|S \cdot R| \cos(2\pi f_x x + \Delta\phi) \right) \cdot \exp\left(-\frac{x^2}{W^2} \right) \quad (3.1.5)$$

Where $f_x = n_0 d / (2L\lambda_0)$, $W = 4\pi L\lambda_0 / (n_0 \Delta)$. Placing waveguides along the output plane serves to sample the diffraction pattern- this is the spatial oversampling discussed in section 2.5. The sampling points needed to satisfy the condition of equation (2.4.3) are:

$$x_n = \left(\frac{2n - N - 1}{2N} \right) \frac{1}{f_x} \quad n = 1, \dots, N \quad (3.1.6)$$

Figure 8 shows the placing of input and output waveguides, as well as the power distribution on the two planes.

The power collected by each output waveguide can be found using an overlap integral of the waveguide mode and the output plane field distribution. In order to gather as much optical power as possible, the output waveguide should cover all of the diffraction pattern. This means their width will be $1/(Nf_x)$. Approximating the modes as Gaussian, and assuming the cosine term of equation (3.1.5) changes slowly over a waveguide's width, the power coupling is:

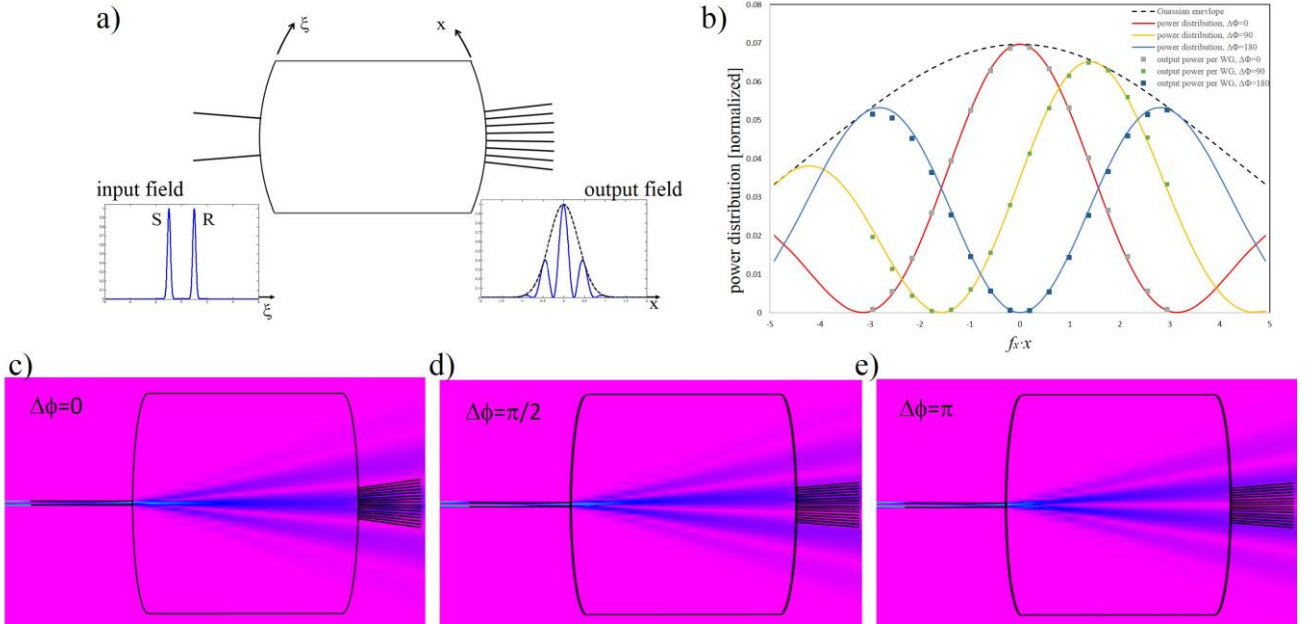


Fig. 8- Geometry of a star coupler and power distribution at the input/output planes. a) layout of star coupler. b) Field distribution at output plane for various input phases. Lines represents the field distribution and markers represent the power gathered by each waveguide. The dashed line is the Gaussian envelope of Equation 3.1.7. c-e) Simulations of 16-outputs star coupler, showing power distribution throughout the device for various input phases. Blue colour represents high power, pink is low power.

$$A_n = \int_{-\infty}^{\infty} \exp\left(-\frac{x^2}{W^2}\right) \exp\left(-\frac{f_x^2 N^2 (x-x_n)^2}{4}\right) dx \approx \frac{2\sqrt{\pi}}{f_x N} \exp\left(-\frac{x_n^2}{W^2}\right) \quad (3.1.7)$$

$$P_n \propto A_n \cdot \left(|R|^2 + |S|^2 + 2|S \cdot R| \cos\left(2\pi \frac{n}{N} + \Delta\varphi\right) \right)$$

From the Gaussian envelope term in equation (3.1.7), we see that some power imbalance between the channels is inherent in this design. There exist a tradeoff between channel imbalance and the total power collected. The ratio between the input waveguides pitch and width determines both the channel imbalance and the total power collected. A low ratio means that the Gaussian envelope is relatively flat, incurring less imbalance. However, this also means that the energy is spread further from the output waveguides, increasing excess loss. Figure 9 shows this tradeoff.

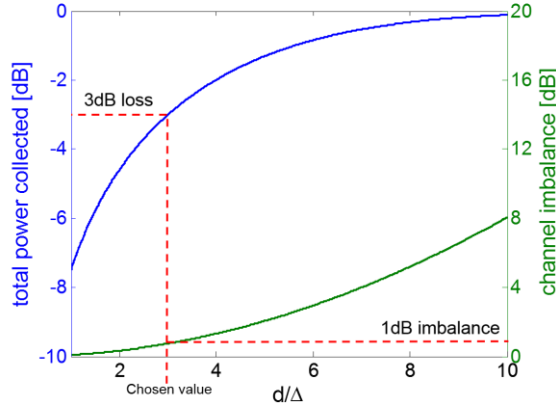


Fig. 9- Total power collected (blue, left axis) and maximal channel imbalance (green, right axis), as a function of the ratio of mode width and pitch of the input waveguide (Δ/d). Presented here for the case of a 45° hybrid ($N=8$). For finer hybrids, the imbalance increases more rapidly. Chosen work point in fabricated devices and corresponding values are shown in dashed lines.

As described in section 2.3, each pair of outputs are fed to a balanced detector. Given the power coupling of equation (3.1.6), the photocurrents of these detectors will be:

$$I_n = \frac{2\sqrt{\pi}}{f_x} \left(\exp\left(-\frac{x_n^2}{W^2}\right) + \exp\left(-\frac{x_{n+N/2}^2}{W^2}\right) \right) \cdot \frac{4}{N} \Re|S \cdot R| \cos\left(2\pi \frac{n}{N} + \Delta\varphi\right) + \frac{2\sqrt{\pi}}{Nf_x} \left(\exp\left(-\frac{x_n^2}{W^2}\right) - \exp\left(-\frac{x_{n+N/2}^2}{W^2}\right) \right) (|R|^2 + |S|^2) \quad (3.1.8)$$

$$I_n = a \frac{4}{N} \Re|S \cdot R| \cos\left(2\pi \frac{n}{N} + \Delta\varphi\right) + I_{DC}$$

This differs slightly for equation (2.4.3). The residual photocurrent I_{DC} can be easily eliminated using an electrical DC-block filter. The proportionality factor, a , is determined by pitch-to-width ratio. In order to provide maximal dynamic range (and hence better SNR) this ratio must be optimized. The optimal working point for the PADC designed was found to be $d/\Delta=5$.

3.2. WDM pulse stream generation

The first step in implementing a time-interleaved photonic ADC using WDM parallelism is to generate a WDM pulse stream. Many methods to accomplish this have been suggested, using a variety of mechanisms. Some implementations use a series of CW laser sources, each modulated using an electro-optic modulator to generate pulses [38-40]. Active solutions such as this use fast electronic modulation sources, and so pulse properties are limited by the electronics. This might cause the timing jitter to be too high. We focus instead on passive methods, where the source is a mode-locked laser and the WDM pulses are created by spectral filtering.

3.2.1 Multiple delay lines

The simplest way to passively generate a WDM pulse stream is to split the signal using a de-multiplexer and passing each spectral channel through a different fiber lengths [11]. Figure 10 shows a schematic layout of such a system. For an overall sampling rate of f_s , the length difference between adjacent channels must be chosen so:

$$\Delta L = cf_s / n \quad (3.2.1)$$

Where n is the fiber's refractive index.

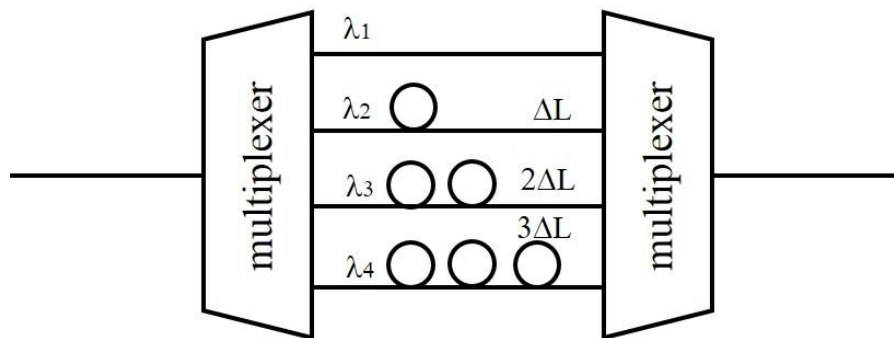


Fig. 10- Schematic layout of wavelength delay system

3.2.2 Linear dispersion and periodic compensation

In the spectral domain, a pulse's arrival time corresponds to its group delay (GD). The narrow pulses of an MLL are characterized by a wide spectrum, with equal phase throughout. Dividing this spectrum into channels and giving each one a different GD will therefore create the desired WDM pulse stream. This type of transfer function can be achieved by cascading a linear wideband dispersion element, such as a grating or an optical fiber, with a periodic dispersion compensation element [41, 42]. If the dispersion slopes for these elements are equal and opposite, the result is a "staircase" GD function, which is the needed transfer function. An

arrayed waveguide grating (AWG), used with a lens and mirror setup, has been shown to provide such tunable optical dispersion compensation (TODC) [43]. Using this element and a free-space grating setup provided a tunable GD staircase, allowing to control the WDM pulse arrivals times, and so controlling the sampling rate. Figure 11 shows the layout and GD functions of this system.

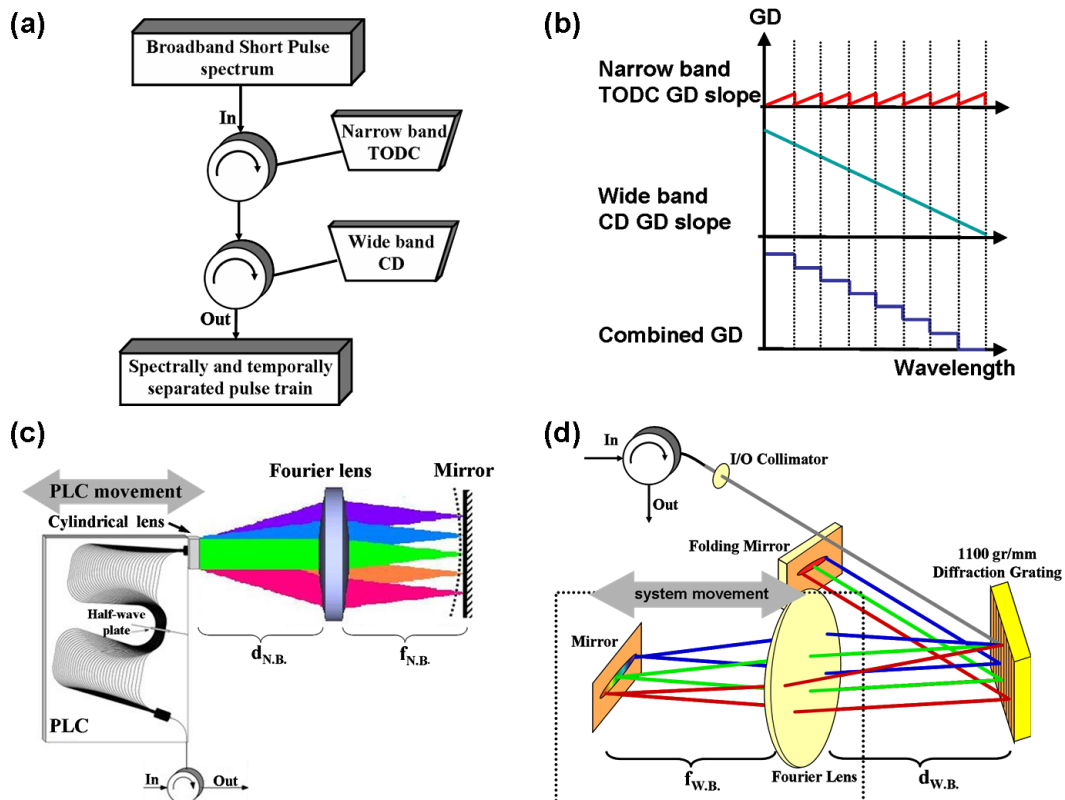


Figure 11 – Layout of the tunable group delay system. (a) The combined setup. (b) The periodic TODC and the linear GD slopes and the combined staircase GD. (c) Periodic TODC setup (d) Wideband CD based on dispersion from a bulk diffraction grating.

3.3. Detection, digitization and DSP

The object of this section is to model each system component, and establish the requirements of the electronic components. We start with the optical parts of the system, ignoring for now time interleaving by WDM pulses. As described in section 2.2, the finite pulse width can be modeled as a low-pass filter. The electro-optic modulator also has a cutoff frequency. Thus the optical sampling process can be modeled as:

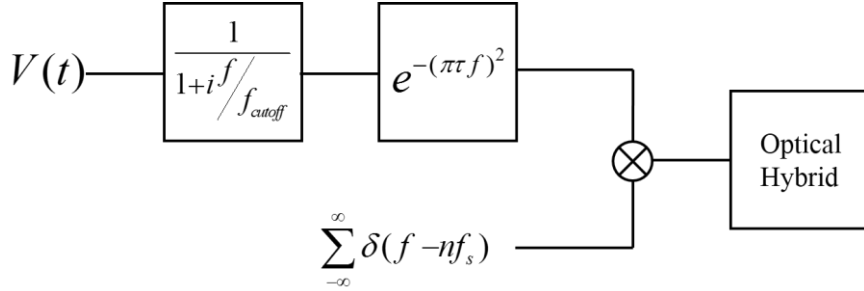


Fig. 12- Block diagram of the electro-optical front end

The sampling process determines the PADC's bandwidth. To ensure a maximal bandwidth at minimal requirement from the optical pulse source, the cutoff frequency defined the pulse width (Equation 2.3.7) should match that of the modulator. The pulse width should be chosen so:

$$\tau \leq \frac{\ln 2}{4\pi} \cdot \frac{1}{f_{cutoff}} \quad (3.3.1)$$

This may be a tough criterion to match- for a modulator bandwidth of 40GHz, 1ps pulses are needed. While this is well within the capabilities of mode-locked lasers, it might make WDM time interleaving more difficult. An easier criterion will be choosing the bandwidth to meet the Nyquist frequency. This determines the pulse width to be:

$$\tau \leq \frac{\ln 2}{2\pi} \cdot \frac{1}{Mf_s} \quad (3.3.2)$$

Here M is the WDM multiplication factor, so that $M \cdot f_s$ is the time-interleaved sampling rate.

While the bandwidth is determined solely by the optical front-end, the maximal sampling rate is determined by the electronics. The analog electronic components of the system are the balanced detectors, amplifiers, integrate-and-hold circuits and electrical ADCs. Figure 13 shows a block diagram of the electronic and digital parts of the system. The balanced detectors are modeled as ideal current source, with a low-pass filter to model their limited bandwidth. The signal is then amplified to meet the full-scale voltage of the ADCs. The amplifier gains may be different for every path, in order to compensate for power imbalance.

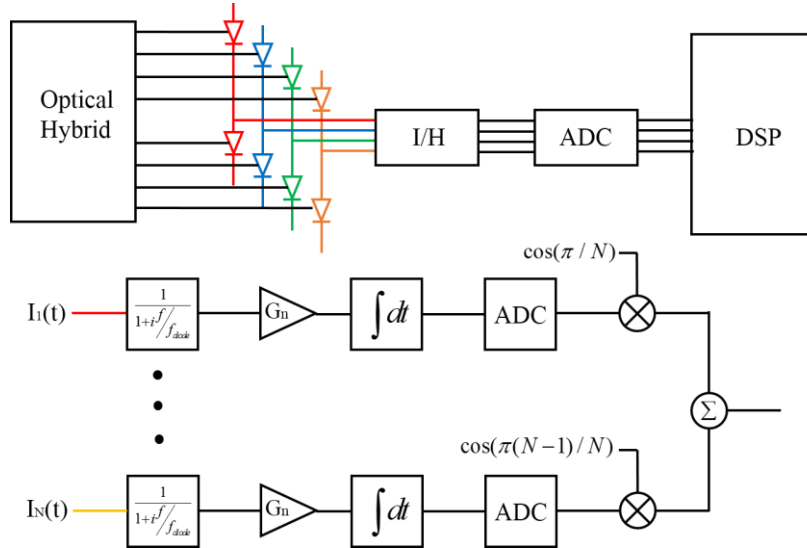


Fig. 13- Block diagram of the analog electronics quantization system

The ADC's sampling rate must be equal to the non-interleaved pulse rate, and the bandwidth and timing of the I/H circuit should be chosen to alleviate its timing requirements. The key requirement is that the output of the S/H will remain constant during the quantization process. This must take into account both the ADC's hold time and any clock jitter of the digital circuitry.

$$t_{S/H} \geq T_{ADC} + \tau_{jitter} \quad (3.3.3)$$

The remaining time can be allocated to integration over the input pulse (the circuit's rise time) and clearing the S/H after quantization takes place, to prepare for the next pulse.

The bandwidth of the combined photodiode and I/H circuit determines the rise/fall time. The optical pulse is very short compared to any time constant of the circuit, and thus the circuit's impulse response is the factor to be considered. Assuming the I/H bandwidth is matched to that of the photodiode, this bandwidth must be chosen so:

$$\frac{1}{f_{diode}} \cong t_{rise} + t_{fall} = T_S - t_{S/H} \quad (3.3.4)$$

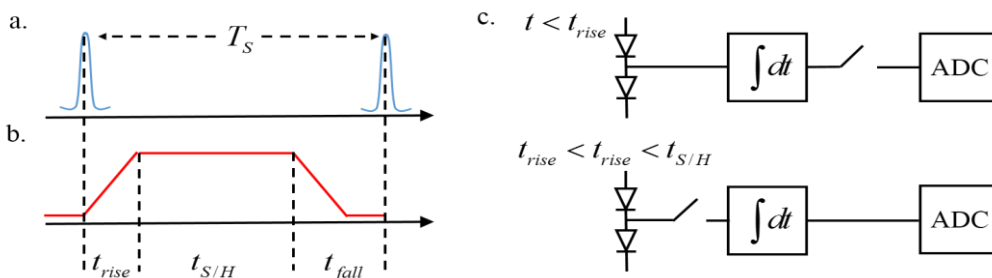


Fig. 14- Illustration of integrate and hold process. a- input pulses at the optical domain. b- I/H circuit output and c- circuit behaviour at different parts of the quantization cycle.

3.4. Noise analysis

As discussed in section 2.4, the use of spatial oversampling can be used to improve detection fidelity, given a set of noisy measurements. This section explores various noise sources that might afflict the system, the effect of oversampling factor on these noises, and the optical power requirements needed for a desired PADC resolution. The noise sources can be separated to optical and electrical noise sources. Optical noise sources include laser source amplitude/phase noise and amplified spontaneous emission (ASE) from optical amplifiers that are used to boost the signal prior to sampling. The electrical sources are shot, thermal and quantization noise.

Starting with the optical noise sources, the optical peak power at the PADC input is:

$$P = P_0 + P_{ASE} + p_l \quad (3.4.1)$$

Where P_0 is the peak pulse power, after amplification, P_{ASE} is the amplified spontaneous emission power and p_l is the change in laser output, which is a Gaussian random process. Using the self-coherent scheme, phase noise is eliminated. This power is split equally, one part serves as reference and the other as phase modulated signal. Therefore:

$$R = \sqrt{\frac{P}{2}}, \quad S = \sqrt{\frac{P}{2}} \cdot e^{i\Delta\phi} \quad (3.4.2)$$

The path differences between signal and reference is very small, and therefore both signal and noise may added coherently. From equation (3.1.7), the power at the n 'th output of the optical hybrid is:

$$P_n = A_n \cdot \left(|R|^2 + |S|^2 + 2|S \cdot R| \cos \left(2\pi \frac{n}{N} + \Delta\phi \right) \right) = A_n P \cdot \left(1 + \cos \left(2\pi \frac{n}{N} + \Delta\phi \right) \right) \quad (3.4.3)$$

After balanced detection, we remain with the photocurrents:

$$I_n = a \frac{4}{N} \Re(P_0 + P_{ASE} + p_l) \cos \left(2\pi \frac{n}{N} + \Delta\phi \right) + \Re(P_0 + P_{ASE} + p_l) (A_n - A_{n+N/2}) \quad (3.4.4)$$

Note that I_{DC} from equation (3.1.8) is replaced with a noisy term. This cannot be simply eliminated with a DC block. While the laser power drift p_l has a bandwidth of order of a few KHz and can be eliminated using a high-pass filter, ASE noise's bandwidth is the same as the electrical circuit's bandwidth [44] and cannot be filtered out. However, as the channel imbalance is small, this noise component is much smaller than the remaining noise terms (on order of 10dB less).

The I/Q terms are both proportional to the input optical power. Therefore, for optical noise limited system, the I/Q SNR is equal to the OSNR. The power level is translated directly to amplitude in the complex I/Q plane. For phase-only modulation it is possible to normalize these terms, so that $I^2 + Q^2 = 1$, removing all amplitude noise. Thus, the self-coherent phase modulation scheme can be said to be immune to optical noise.

From equation (2.4.3), we find the RMS photocurrent in each balanced detector. Ignoring excess loss and channel imbalance, and assuming the input voltage cover the full range equally, this is:

$$\bar{I}_n = \frac{4}{\sqrt{2N}} \Re P_0 \quad (3.4.5)$$

For a fine resolution ADC with an ENOB of B , quantization errors can be modeled as a random variable, uniformly distributed on a $[0, 2^{-B}]$ range [45]. This is scaled by the full-scale voltage of the ADC. This requires that the full-scale voltage of the I/H circuit is matched to that of the ADC, which can be accomplished by using trans-impedance amplifiers, as shown in figure 13. The detection adds shot noise and thermal noise, and so the electric noise power are:

$$\begin{aligned} \bar{I}_{shot}^2 &= q\bar{I}_n\Delta f = \frac{4}{\sqrt{2N}} \Re P_0 q\Delta f \\ \bar{I}_{thermal}^2 &= 4 \frac{K_B T}{r} F_n \Delta f \\ \bar{I}_{quant}^2 &= \frac{I_{fs}^2}{12} 2^{-B} = \left(\frac{4}{N} \Re P_0 \right)^2 \cdot \frac{1}{12} 2^{-2B} \end{aligned} \quad (3.4.6)$$

Where r is the circuit's resistance, F_n the trans-impedance amplifier's noise figure, B the ADC's resolution in bits and Δf the circuit's electrical bandwidth. The single-detector SNR is therefore:

$$SNR_n = \frac{\bar{I}_n^2}{\bar{I}_{shot}^2 + \bar{I}_{thermal}^2 + \bar{I}_{quant}^2} = \left(\frac{\sqrt{2}Nq\Delta f}{4\Re P_0} + \frac{N^2 K_B T F_n \Delta f}{2r(\Re P_0)^2} + \frac{2}{12} 2^{-2B} \right)^{-1} \quad (3.4.7)$$

These noise terms are independent for every detector, and therefore meet the conditions for spatial oversampling noise improvement, as discussed in section 2.4. Using equation (2.5.9) we get the phase-estimation SNR:

$$SNR_\phi = \frac{\pi^2 N}{4} \cdot SNR_n = \pi^2 \left(\frac{\sqrt{2}q\Delta f}{\Re P_0} + \frac{NK_B T F_n \Delta f}{8r(\Re P_0)^2} + \frac{8}{N} \frac{1}{12} 2^{-2B} \right)^{-1} \quad (3.4.8)$$

Equation (3.4.7) shows the condition in which oversampling is beneficial. For the case of shot noise limited system the first term in the parenthesis dominates, and the SNR does not change with the choice of optical hybrid. For a thermal noise limited system the second term is most significant. In this case performance degrades as the oversampling factor increases, because the penalty of splitting the power is more significant than the benefit of oversampling. For quantization noise limited system the third term dominates, and performance scales with N . This is the case of highest interest, where:

$$ENOB_{\phi} = \frac{SNR_{\phi} - 1.76}{6.02} = \frac{1}{2} \log_2(\pi^2 N \cdot 2^{2B}) = B + \frac{1}{2} \log_2 N + \log_2(\pi) \quad (3.4.9)$$

Note that this is identical to equation (2.5.10) which was our goal.

4. Experimental results

4.1. WDM pulse stream generation

Generation of a WDM pulse stream was accomplished using the system described in section 3.2.2- cascading a linear GD module with periodic dispersion correction. Design and measurement of this setup was not a part of this thesis, and these results are brought here for completeness, as this subsystem is essential for overall system performance. A full description of this system and measurements can be found in [41].

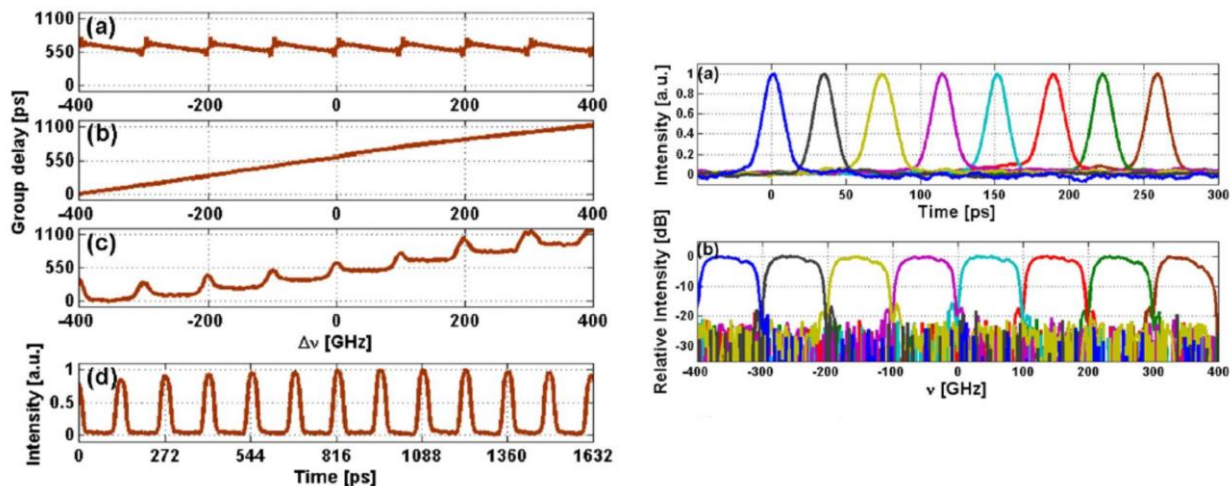


Fig. 15- Generation of WDM pulse stream from a MLL source. (Left) GD transfer function of periodic element (a), linear GD module (b) and combined system (c). d) Resulting pulse stream, starting from a MLL source. (Right) Demonstration of the polychromatic nature of the stream, obtained by measuring each WDM sub-channel individually. a) shows the pulses in time, b) shows each pulse's spectrum.

4.2. Star-coupler fabrication and characterization

The optical hybrids were fabricated in the form of a planer lightwave circuit (PLC), using silica on silicon technology. The devices were produced at Bell Labs Alcatel-Lucent fab. Rectangular waveguide were used, with cores were made of $\text{Si}_x\text{Ge}_{1-x}\text{O}_2$ (refractive index of 1.47) and the cladding of SiO_2 (refractive index of 1.44). Core thickness was $4\mu\text{m}$, and cladding width of $28\mu\text{m}$. $750\mu\text{m}$ thick Silicon substrate provides mechanical stability. $4\times 4\mu\text{m}$ waveguides of this type are single-mode in telecom wavelengths, with an effective index of 1.46.

Three type of star-couplers were produced, with 8, 12 and 16 output ports, suitable for 45° , 30° and 22.5° optical hybrids, respectively. Minimal waveguide distance allowed by the manufacturer was $1.5\mu\text{m}$, due to fabrication process limitations. This is important mainly in the output facet of the star-coupler, as the waveguides cannot fill the whole space. This causes an increase in device losses, approximately equal to the ratio of gap width to waveguide width.

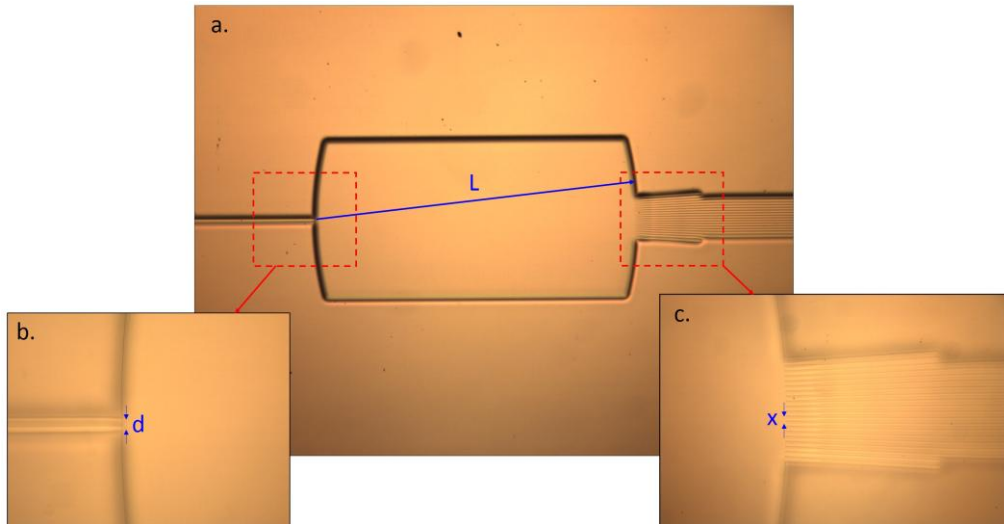


Fig. 16- microscope images on 2x16 star coupler. a. slab lens layout. b. zoom in on input plane. c. zoom in on

For this ratio (and therefore the losses) to be equal in all star-couplers, the slab lens radius was changed for each device, and so the output waveguide width remained constant. Figure 16 shows microscope image of the interference region of one of the fabricated star-couplers ($N=16$).

Waveguides dimensions and pitch are:

- Input waveguide pitch (d): $10\mu\text{m}$
- Input waveguide width (W): $4\mu\text{m}$
- output waveguide pitch: $10\mu\text{m}$
- Output waveguide width: $8.5\mu\text{m}$ (adiabatically narrowed to $4\mu\text{m}$)
- Slab lens radius (L): $752\mu\text{m}$, $1128\mu\text{m}$, $1504\mu\text{m}$ for 8, 12, and 16 output ports respectively.

4.3. Spatial oversampling without optical sampling

In order to demonstrate the concept of spatial oversampling in a simple system, as well as characterizing star-couplers' performance, a simpler version of the system was first constructed. The star-couplers were connected to optical fiber inputs (no direct assembly with the LiNbO_3 modulator), and a CW source was used. An input CW laser was split with a 50/50 fiber splitter, and one arm was input to an external phase modulator. The modulated and unmodulated arms were then input to the star couplers. Outputs were detected using balanced detectors, as described in section 2.4. A 10MHz $10V_{pp}$ sine wave was applied to the modulator, and the system resolution was evaluated. This experiment was performed for 90° , 45° , 30° and

22.5° optical hybrids ($N=4, 8, 12$ and 16 , respectively), and the SNR improvement was estimated. To ensure that the system was quantization-noise limited, a 4 ENOB quantizers were used. Figure 17 shows the measured SNR improvement caused by spatial oversampling. A 3dB improvement was observed for doubling N , as predicted by equation 2.5.10. These results were

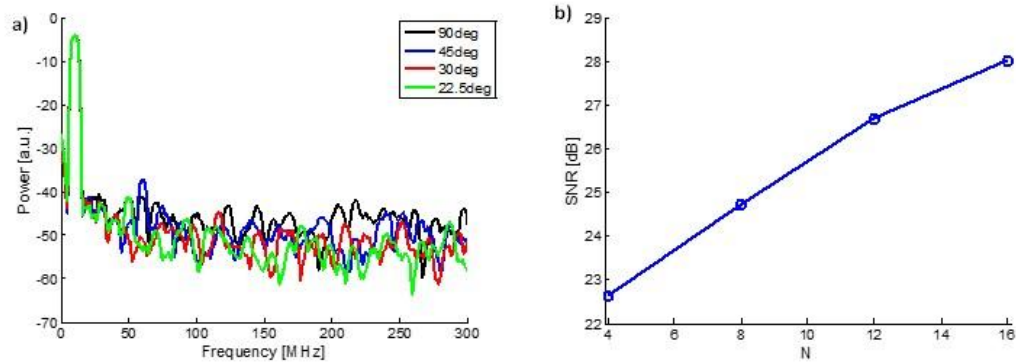


Fig. 17- Effect of spatial oversampling. a) Power spectrum of estimated phase. b) SNR provided by each optical hybrid, showing a linear increase in SNR with increasing the number of output ports N .

reported on in [46].

4.4. Phase modulator and star-coupler integration

Constructing the photonic ADC with a standard commercial phase modulator will require optical fiber connecting the modulator and the optical hybrid. This means a relatively long fiber interferometer, resulting in significant phase drift for each output port. To prevent this problem custom made modulators were used, designed to interface directly with the silica PLCs that hold the star-couplers. The modulators were Titanium-diffused LiNbO₃ modulators, produced by Oclaro Inc. The electro-optic bandwidth was 40GHz and half-wave voltage $V_{\pi}=5.5V$. Tapered waveguides were used on the input of the silica PLC, in order to provide maximal coupling with the LiNbO₃ chip. The mode size was optimized, and the optimum was found to

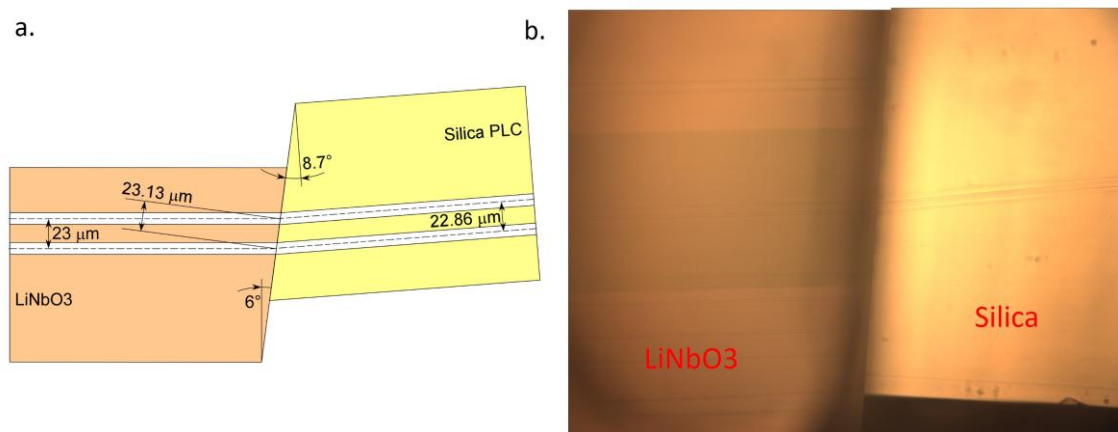


Fig. 18- Modulator-PLC interface. a. Layout of interface area. b. microscope image of the connected devices

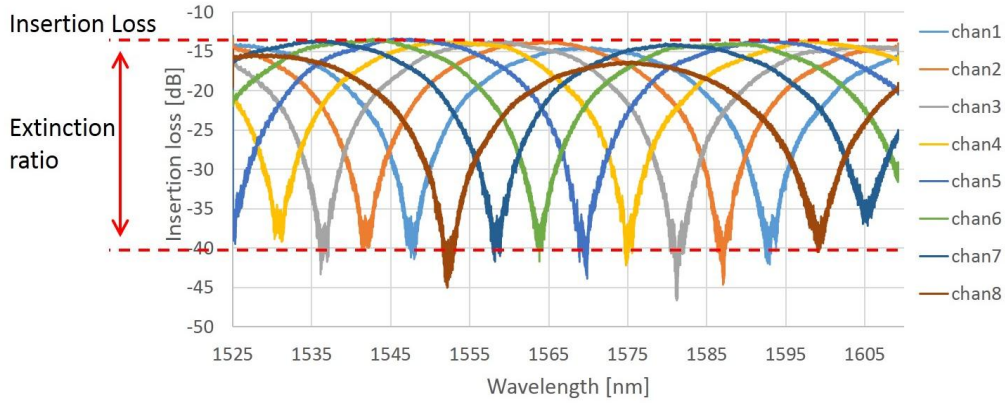


Fig. 19- LUNA measurements used to characterize an integrated modulator and 8-port star coupler

be $10.6\mu\text{m}$ wide waveguides on the PLC side. To prevent reflections, the LiNbO_3 chip was cut at a 6° angle and the PLC at a 8.7° angle. Figure 18 shows the layout of the chip interface and a microscope image of it.

The coupling coefficients between the modulator’s input and each of the outputs is dependent on the input RF voltage. Therefore three parameters are required to characterize the response of each output port: maximal coupling, extinction ratio and phase offset. These were measured using a LUNA optical vector analyzer. An example of such measurement can be seen in figure 19. The measured parameters for all of the devices are in appendix A.

In order to determine the impact of phase drift, a sinusoid RF signal and CW laser source were applied to the integrated modulator-star coupler. The outputs were measured using balanced detectors and an oscilloscope. The signals were accumulated over 10 minutes, in an uncontrolled environment (i.e. no temperature control or shielding from the surroundings). No significant phase drift was observed over this time length. Figure 20 shows the results of this measurement.

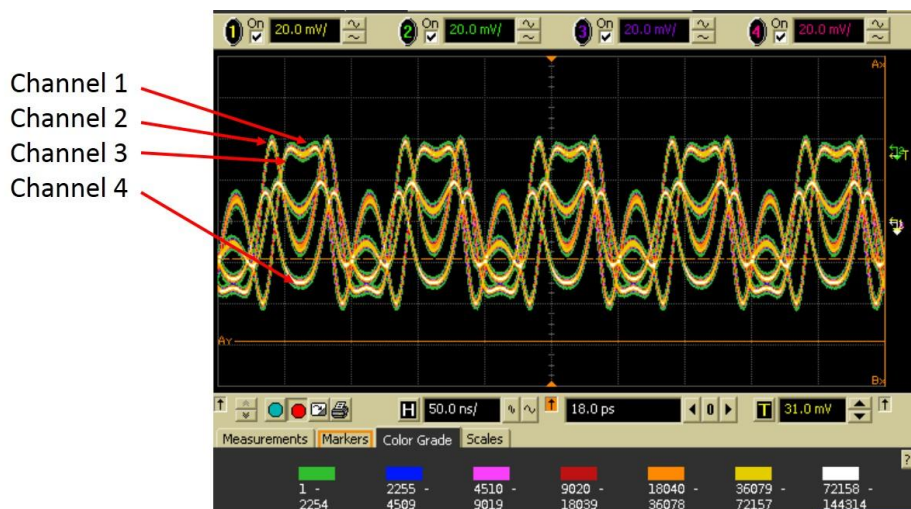


Fig. 20- measured star-coupler output, with input CW laser and a 10MHz 10Vpp sine wave, accumulated over 10 minutes

4.5. Experimental setup

4.5.1. Increasing pulse rate

A mode-locked laser was used for optical sampling. The MLL provided 100fs pulses, with a repetition rate of 80MHz, timing jitter of 300fs and average optical power of ~24dBm (this value changed between different measurements, in the 23-24.7dBm range). As the sampling rate was insufficient, a free-space delay lines configuration was used (figure 20). The delay lines split the pulse stream, and combine it with different optical paths. This creates an aggregated pulse rate, so that the output pulse rate is:

$$f_{\text{samp}} = f_{\text{MLL}} \cdot 2^M \quad (4.5.1)$$

Where f_{MLL} is the MLL's repetition rate and M is the number of delay lines. Using this setup, the pulse rate was increased to 1.28GHz (4 delay lines). Setting the delay lines length allowed tweaking with pulse arrival times, and adjusting the mirrors and beams splitters allowed equalizing pulse amplitudes. However, finite detection resolution limited the ability to determine the pulse arrival times to an error of several picoseconds, and the complexity of the setup prevented full amplitude equalization- differences of up to 1dB remained. Figure 21b

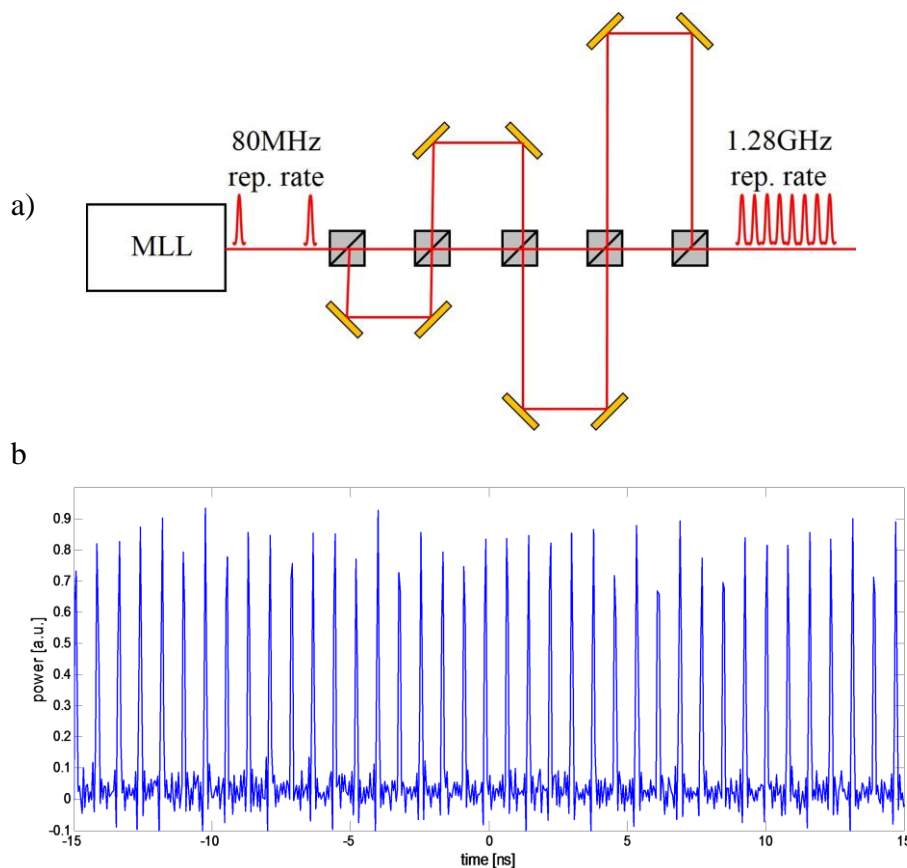


Fig. 21- a) Delay lines setup, for increasing MLL pulse rate. b) 1.28GHz pulse stream at setup output.

shows the output of the delay lines setup. These timing and amplitude errors inhibit the performance of the PADC system, and must be compensated for. This was done digitally, by considering the digitized values as 16 interleaved sets, correcting each one individually, and merging the results into one stream.

4.5.2. Synchronizing modulation and pulses

A full PADC system WDM sampling require many detectors and ADCs. The experimental system, used here as proof as concept, is composed of discrete components (not in the form of integrated electronics) and so cannot support the full number of detectors and ADCs required. This means that each WDM channel must be detected separately, using the same set of detectors for all wavelengths. This cause a problem of synchronizing the input signal with the sampling pulses: as the measurements take place at different times, the signal will have a different time offset in respect to the pulses for each wavelength. This will prevent combining the wavelength channels to a single stream. To prevent this problem, the signal must be synchronized to the MLL. This was achieved by using the MLL pulses as a signal source. The MLL's idler signal is detected. The detected signal contains many harmonics of the fundamental MLL frequency (80MHz). Using an ultra-narrow bandpass filter, a single harmonic line is obtained, providing a single tone that is perfectly synchronized with the sampling pulse stream. Two filters were used, providing signal at 2.96GHz and 8GHz (37th and 100th harmonic of the fundamental rate).

Figure 22 shows the full experimental system, used to obtain the results in the next section.

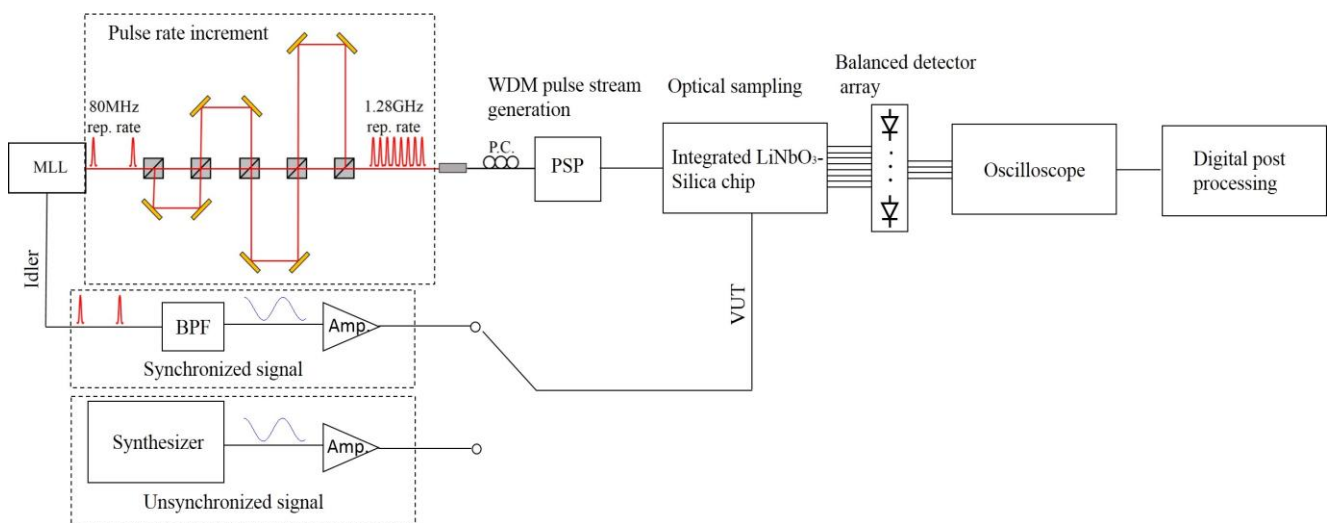


Fig. 22- Experimental setup used to test PADC performance. Two types of signal were used- synchronized signals (as described in 4.2.2) and unsynchronized (generated by a synthesizer and not synchronized with the sampling pulses).

4.6. PADC results

The PADC system was tested by applying several modulation signals, performing the detection/digitization process, and comparing the results to the known input. The following section contains some examples of these measurements.

4.6.1. Linear sweeps

Slow linear voltage sweeps were performed as a way to calibrate the system, i.e. finding the measurement voltages corresponding to various input voltages. This measurement enables to cancel out the effects of amplitude/offset differences between the channels, caused by differences between detectors and channel mismatches. Figure 23 shows several stages in such a measurement. The input signal was a $10V_{pp}$ 100KHz voltage ramp, corresponding to a phase modulation depth of 1.75π .

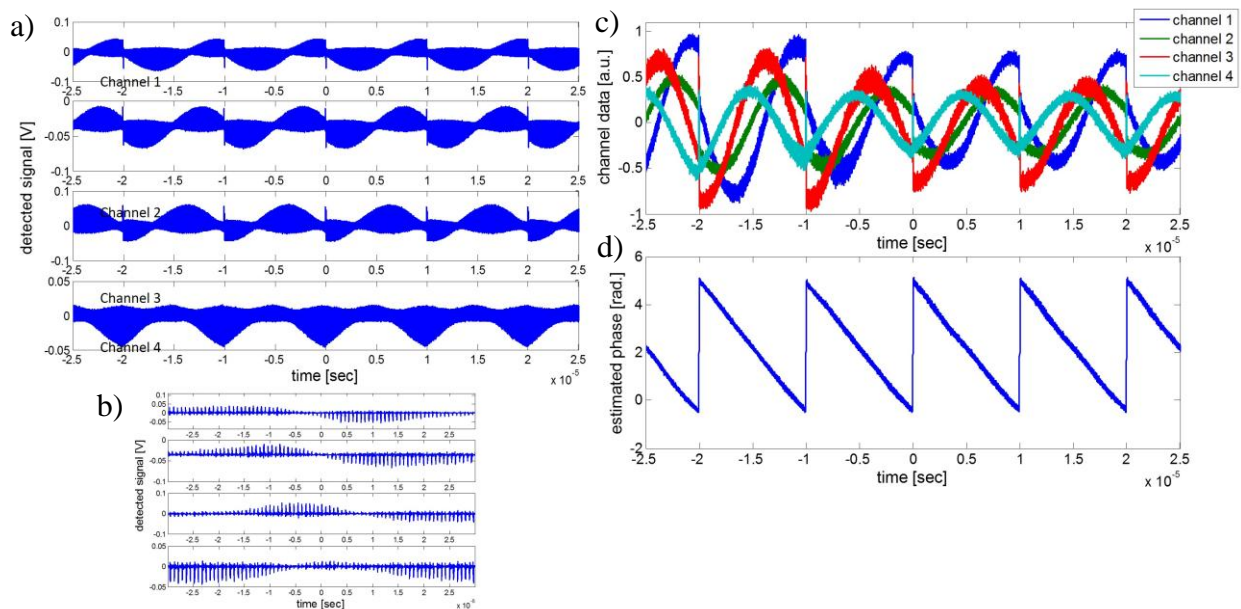


Fig. 23- Measurement results for linear sweep input, digitized by 1.28GHz pulse stream and a 2-oversampled PADC. a) Detected pulses for all four channels. b) Zoom in on detected pulses c) Data carried by each channel (output of I/H subsystem). d) Estimated phase, corresponding to input voltage.

4.6.2. Low frequency sine wave

Low frequency sine wave was input to examine system resolution limit. At modulation frequencies well below the MLL's fundamental pulse rate, phase errors caused by delay lines timing errors become insignificant. System resolution was extracted by fitting the result to an ideal sine wave, and was shown to be 6 ENOB. The input signal was a $10V_{pp}$ 10MHz sine wave. The modulation covered only 1.75π of the 2π maximal modulation depth, and so the full scale resolution is projected to be 6.8 ENOB.

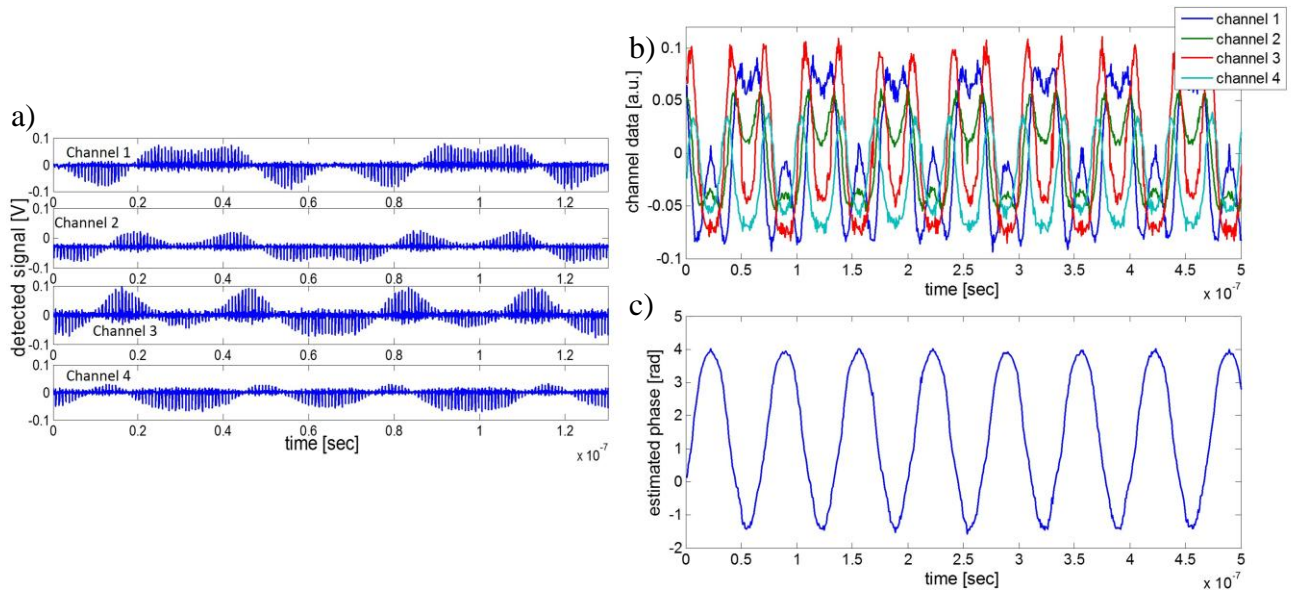


Fig. 24- Measurement results for 10MHz sine wave, digitized by 1.28GHz pulse stream and a 2-oversampled PADC.
a) Detected pulses for all four channels. b) Data carried by each channel (output of I/H subsystem). c) Estimated phase, corresponding to input voltage.

4.6.2. High frequency sine wave

High frequency sine wave was input to examine system behavior at target frequencies of several GHz. At these frequencies, the signal is heavily undersampled (1.28GS/s, while the required sampling rate for Nyquist ADC is $>20\text{GS/s}$). Two main differences exist from the low-frequency case: the signal (and any potential harmonics introduced by the modulator) is aliased; delay lines timing errors cause significant phase errors, which must be digitally corrected. The types of correction used and their effects for various signals are explained in appendix B. Two methods of phase estimation were used; one utilizing all four detected signals and one utilizing only two. The latter is equivalent to using a standard 90° optical hybrid. For both methods, system resolution was extracted by fitting the result to an ideal sine wave, and was shown to be 5 ENOB for the 90° configuration and 5.4 ENOB for the 45° configuration. This shows a resolution improvement of approximately 0.4 ENOB when increasing N from 4 to 8, a very close result similar the theoretical one (0.5 ENOB improvement). The input signal was a $6V_{pp}$ 12.9GHz sine wave, covering approximately half of the dynamic range. The full scale resolution is therefore projected to be 6.3 ENOB. Figure 25 shows the results of this measurements, as well as the importance of correcting for phase errors.

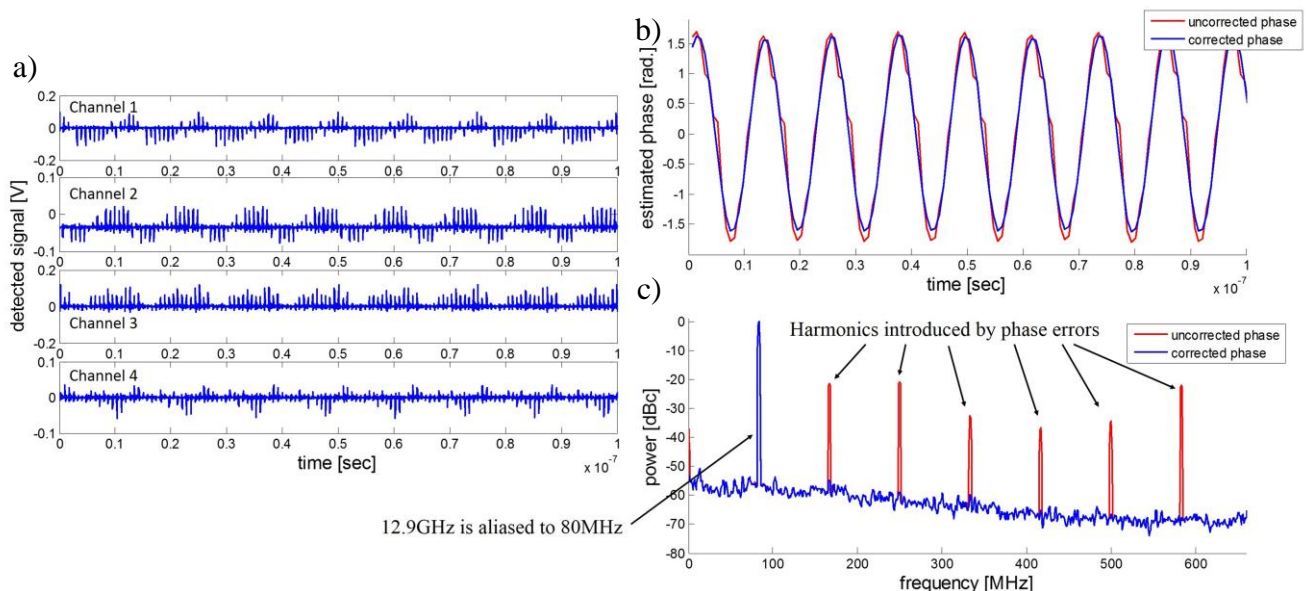


Fig. 25- Measurement results for 12.9GHz sine wave, digitized by 1.28GHz pulse stream and a 2-oversampled PADC. a) Detected pulses for all four channels. b) Estimated phase, with and without phase corrections. c) Power spectrum of estimated phase.

5. Conclusion and discussion

This work explored the concepts of photonic analog to digital conversion and spatial oversampling. Spatial oversampling is, in essence, an averaging method that can help reduce noise in optical coherent detection. This work focused on its application to photonic ADCs, but the concept itself is more general. Fine optical hybrids can be used to improve coherent detection in optical communication systems using the same methods described in section 2.4. As the principles of spatial oversampling are general and do not apply to optics alone, this concept can be exported to other fields (e.g. RF electronics), with the only difference is in replacing the fine optical hybrid with a multi-output mixer.

Theoretical and experimental proofs of the ability of the spatial oversampling technique to improve ADC resolution are presented. The photonic ADC presented here showed a resolution of 6.3 ENOB, ranking among the highest photonic ADCs presented so far. System performance can be greatly improved by using better electronics- dedicated ADCs will perform better than the oscilloscope used to acquire the results in section 4, and using suitable filters will remove noise and simplify the required digital processing.

While it is technically possible to design a photonic ADC with an arbitrarily high spatial oversampling factor, it is important to note the increase in system complexity and cost. Halving noise incurs doubling the complexity, and the exact optimum of this trade-off must be determined according to the application in which the photonic ADC is used. In practice, an oversampling factor of 2-4 seems feasible (a 1 ENOB boost to resolution).

For these concepts to find commercial application, two main drawbacks must be addressed. Currently, most photonic ADCs use a mode-locked laser as a sampling pulse source. While these provide the lowest jitter and highest stability, they are also very large and expensive. A more compact optical pulse source must be developed for practical realizations of a photonic ADC. Second, the photonic ADC require many detectors and sub-ADCs in parallel. Current implementation use discrete components, which makes implementing the full system impractical. Large scale integration is required for the system to be viable. This work showed the beginning of integration- the optical hybrids and photonic spectral processors are already implemented as a photonic integrated circuit. The next step is to design designated electronic circuits, featuring the necessary amount of detectors and ADCs on a single board. This is purely a technical problem, as the required technology already exists. A collaborative work of the photonic and electronic communities can make commercial photonic ADCs possible, providing unprecedented bandwidth and resolution.

6. References

1. R.H. Walden, "Analog-to-Digital Converters Survey and Analysis", IEEE Selected Areas in Communications, vol.17, no.4, pp.539-550, (1999)
2. S. Gupta, M. Choi, M. Inerfield, Jingbo Wang, "A 1GS/s 11b Time-Interleaved ADC in 0.13/ μm CMOS", ISSCC 2006., pp.2360-2369, (2006)
3. N. Kurosawa, H. Kobayashi, K. Maruyama, H. Sugawara, K. Kobayashi "Explicit analysis of channel mismatch effects in time-interleaved ADC systems," IEEE Circuits and Systems I: Fundamental Theory and Applications, vol.48, no.3, pp.261-271, (2001)
4. M. Macedo, G.W. Roberts, S. Ishiang, "Track and hold for Giga-sample ADC applications using CMOS technology," ISCAS 2012, pp.2725-2728, (2012)
5. G.C. Valley, "Photonic Analog-to-Digital Converters", Optics Express, Vol. 15, Issue 5, pp. 1955-1982 (2007)
6. J. Sauerbrey, D. Schmitt-Landsiedel, R. Thewes, "A 0.5-V 1- μW successive approximation ADC," IEEE Journal of Solid-State Circuits, vol.38, no.7, pp.1261-1265, (2003)
7. K. Poulton, J.J. Corcoran; Thomas Hornak , "A 1-GHz 6-bit ADC system," IEEE Journal of Solid-State Circuits, vol.22, no.6, pp.962-970, (1987)
8. T.M. Souders, Donald R. Flach, C. Hagwood, G.L. Yang, "The effects of timing jitter in sampling systems," IEEE Transactions on Instrumentation and Measurement, vol.39, no.1, pp.80-85, (1990)
9. B. Murmann, "ADC Performance Survey 1997-2013," ISSCC 2013
10. K. Takizawa, and M. Okada, "Analog-to-digital converter: a new type using an electrooptic light modulator," Applied Optics, 18, 3148-3151 (1979).
11. A. Khilo, S. J. Spector, M. E. Grein, A. H. Nejadmalayeri, C. W. Holzwarth, M. Y. Sander, M. S. Dahlem, M. Y. Peng, M. W. Geis, N. A. DiLello, J. U. Yoon, A. Motamedi, J. S. Orcutt, J. P. Wang, C. M. Sorace-Agaskar, M. A. Popović, J. Sun, G.-R. Zhou, H. Byun, J. Chen, J. L. Hoyt, H. I. Smith, R. J. Ram, M. Perrott, T. M. Lyszczarz, E. P. Ippen, and Franz X. Kärtner, "Photonic ADC: overcoming the bottleneck of electronic jitter", Optics Express, Vol. 20, Issue 4, pp. 4454-4469 (2012)
12. A. H. Nejadmalayeri, M. E. Grein, A. Khilo, J. Wang, M. Y. Sander, M. Peng, C. M. Sorace, E. P. Ippen, and F.X. Kaertner, "A 16-fs aperture-jitter photonic ADC: 7.0 ENOB at 40 GHz", CLEO 2011

13. C. W. Holzwarth, R. Amatya, M. Araghchini, J. Birge, H. Byun, J. Chen, M. Dahlem, N. A. DiLello, F. Gan, J. L. Hoyt, E. P. Ippen, F. X. Kärtner, A. Khilo, J. Kim, M. Kim, A. Motamedi, J. S. Orcutt, M. Park, M. Perrott, M. A. Popovic, R. J. Ram, H. I. Smith, G. R. Zhou, S. J. Spector, T. M. Lyszczarz, M. W. Geis, D. M. Lennon, J. U. Yoon, M. E. Grein, R. T. Schulein, S. Frolov, A. Hanjani, J. Shmulovich, "High Speed Analog-to-Digital Conversion with Silicon Photonics", Proc. SPIE 7220, Silicon Photonics IV, 72200B (2009)
14. M. E. Grein, S. J. Spector, A. Khilo, A. H. Najadmalayeri, M. Y. Sander, M. Peng, J. Wang, C. M. Sorace, M. W. Geis, M. M. Willis, D. M. Lennon, T. M. Lyszczarz, E. P. Ippen, and F. X. Kärtner, "Demonstration of a 10 GHz CMOS-Compatible Integrated Photonic Analog-to-Digital Converter," CLEO (2011)
15. D. R. Reilly, S. X. Wang, and G. S. Kanter, "Optical Under-Sampling for High Resolution Analog-to-Digital Conversion," Avionics, Fiber- Optics and Photonics Technology Conference (AVFOP), pp.35-36, (2011)
16. Q. Wu, H. Zhang, X. Fu, and M. Yao, "A New Proposal of Spectral Encoded Photonic Analog-to-digital Converter," Microwave photonics Conference, MWP/APMP, pp.247-250, (2008)
17. T. Nishitani, T. Konishi, K. Itoh, "Demonstration of 4-bit Photonic Analog-to-digital Conversion Employing Self-frequency shift and SPM-induced Spectral Compression," 33rd European Conference and Exhibition of Optical Communication (ECOC), (2007)
18. T. Konishi, K. Takahashi, H. Matsui, T. Satoh, "Optical quantization for 6 bit photonic A/D conversion," 14th International Conference on Transparent Optical Networks (ICTON), (2012)
19. H. Matsui, K. Takahashi, T. Konishi, and K. Itoh, "Optical coding by 2-dimensional stacked pulse shapers for 6bit photonic analog-to-digital conversion," Opto-Electronics and Communications Conference (OECC), pp.26-27, (2011)
20. J. Stigwall and S. Galt, "Demonstration and analysis of a 40-gigasample/s interferometric analog-to-digital converter" Journal of Lightwave Technology, vol. 24, no. 3, pp. 1247, (2006)
21. M. Jarrahi, R. F. W. Pease, D. A. B. Miller, T. H. Lee, "Optical Spatial Quantization for Higher Performance Analog-to-Digital Conversion," IEEE Transactions on Microwave Theory and Techniques, vol. 56, no. 9, pp 2143-2150, (2008)

22. W. Li, H. Zhang, Q. Wu, Z. Zhang, and M. Yao, "All-Optical Analog-to-Digital Conversion Based on Polarization-Differential Interference and Phase Modulation," *Photonic Technology Letters*, vol.19, no. 8, pp. 625-627, (2007)
23. M. Nazarathy and O. Shaham, "Spatially Distributed SAR Photonic ADCs based on Phase-Domain Quantization", *Optics Express*, Vol. 20, Issue 7, pp. 7833-7869 (2012)
24. A. S. Bhushan, F. Coppinger, B. Jalali, "Time-stretched analogue-to-digital conversion," *Electronics Letters* , vol.34, no.9, pp.839-841, (1998)
25. A. S. Bhushan, P.V. Kelkar, B. Jalali, O. Boyraz, M. Islam, "130-GSa/s photonic analog-to-digital converter with time stretch preprocessor," *Photonics Technology Letters, IEEE* , vol.14, no.5, pp.684-686, (2002)
26. J.U. Kang, R.D. Esman, "Demonstration of time interweaved photonic four-channel WDM sampler for hybrid analogue-digital converter," *Electronics Letters*, vol.35, no.1, pp.60-61, (1999)
27. R. Kuc, *Introduction to digital signal processing*, McGraw-Hill, New York, (1988)
28. T. D. Gathman, J. F. Buckwalter, "An Integrate-and-Dump Receiver for High Dynamic Range Photonic Analog-to-Digital Conversion," *Silicon Monolithic Integrated Circuits in RF Systems (SiRF)*, pp. 155-158, (2012)
29. Bahaa E.A. Selah and Malvin C. Teich, *Fundamentals of photonics*, Wiley, New York (1991)
30. C. DRAGONE, " Efficient N x N Star Couplers Using Fourier Optics", *Journal of Lightwave Technology*, vol. 7, pp. 479-489, (1989)
31. L. G. Kazovsky, L. Curtis, W. C. Young, N. K. Cheung, "All-fiber 90° optical hybrid for coherent communications", *Applied Optics*, vol. 26, pp. 437-439, (1987)
32. Lucas B. Soldano and Erik C.M. Pennings, "Optical Multi-Mode Interference Devices Based on Self-Imaging: Principles and Applications", *Journal of Lightwave Technology*, vol. 13, pp. 615-627, (1995)
33. Seok-Hwan Jeong and Ken Morito, " Optical 45° hybrid for demodulating 8-ary DPSK signal" *Optics Letters*, vol. 36, pp. 322-324, (2011)
34. Seok-Hwan Jeong and Ken Morito, " Optical 60° hybrid for demodulating six-level DPSK signal", *Optics Express*, vol. 18, pp. 8482, (2010)
35. Christopher R. Doerr, , Douglas M. Gill, Alan H. Gnauck, Lawrence L. Buhl, Peter J. Winzer, Mark A. Cappuzzo, A. Wong-Foy, Evans Yifan Chen, and L. T. Gomez, "Monolithic Demodulator for 40-Gb/s DQPSK Using a Star Coupler", *Journal of Lightwave Technology*, vol. 24, pp. 171-174, (2006)

36. N.G. Walker, J.E. Carroll, "Simultaneous phase and amplitude measurements on optical signals using a multiport junction," *Electronics Letters* , vol. 20, pp. 981-983, (1984)
37. L.R. Carley, "An oversampling analog-to-digital converter topology for high-resolution signal acquisition systems," *IEEE Transactions on Circuits and Systems*, vol.34, no.1, pp.83-90, (1987)
38. J. V. Howe, J. Hansryd, and C. Xu, "Multiwavelength pulse generator using time-lens compression," *Optics Letters*. 29, 1470-1472, (2004)
39. L. Ka-Lun, C. Shu, Hai-Feng Liu, "Subharmonic pulse-gating in self-seeded laser diodes for time- and wavelength-interleaved picosecond pulse generation," *Quantum Electronics*, vol.40, no.3, pp.205,213, (2004)
40. X. Fu, H. M. Zhang, Y. Peng, and M. Y. Yao, "40-Gbps time- and wavelength-interleaved pulse-train generation in wavelength-demultiplexing analog-to-digital conversion," *Optics Engineering*, 48, 104302, (2009).
41. David Sinefeld, Yiska Fattal, and Dan M. Marom, "Generation of WDM adaptive-rate pulse bursts by cascading narrow/wideband tunable optical dispersion compensators," *Optics Letters* 37, 4290-4292, (2012)
42. H. Q. Lam, K. E. K. Lee, and P. H. Lim, "Time- and wavelength-interleaved optical pulse train generation based on dispersion spreading and sectional compression," *Optics Letters*, 37, 2349, (2012).
43. D. Sinefeld, S. Ben-Ezra, C. R. Doerr, and D. M. Marom, "All-channel tunable optical dispersion compensator based on linear translation of a waveguide grating router," *Optics Letters*, 36, 1410-1412, (2011)
44. G.P. Agrawal, *Lightwave Technology- Telecommunication Systems*, (Wiley 2005)
45. R.M. Gray, D.L. Neuhoff, "Quantization," *IEEE Transactions on Information Theory*, vol. 44, pp. 2325-2383, (1998)
46. Ori Golani, David Seinfeld, Shalva Ben-Ezra, and Dan M. Marom, "Fine Optical Hybrids for High-Fidelity Coherent Receivers", *Photonic Technology Letters*, (Submitted)

Appendix A- Measured coupling parameters of integrated star-couplers

The coupling parameters of each star coupler were measured using a LUNA optical vector analyzer. For each output port, the phase offset ($\Delta\phi$) is defined as the phase difference between it and the first output port.

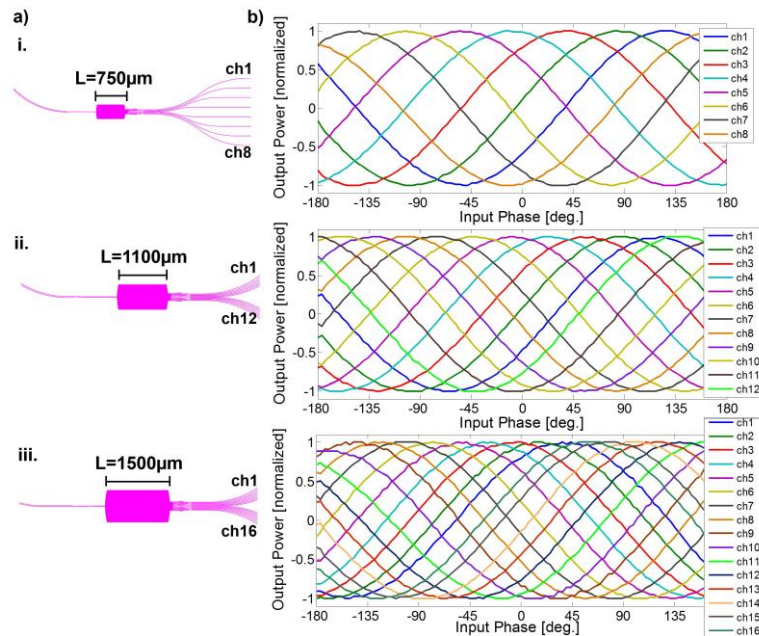


Fig. 26- Measured response of individual output ports to input phase difference

Table 1- measured coupling coefficients for all optical hybrids

Port #	8 output hybrid			12 output hybrid			16 output hybrid		
	Coupling coefficient [dB]	Extinction ratio [dB]	Phase offset [deg.]	Coupling coefficient [dB]	Extinction ratio [dB]	Phase offset [deg.]	Coupling coefficient [dB]	Extinction ratio [dB]	Phase offset [deg.]
1	13	29	0	13.65	29.8	0	15.38	20.8	0
2	13.33	31.2	45.88	12.77	30.02	24.52	15.07	20.9	24.39
3	13.57	33	88.22	12.65	29.14	52.8	14.92	20.44	45.07
4	13.57	28.6	132.45	12.54	27.25	80.2	14.68	20.68	66.71
5	13.32	30.5	191.4	12.43	30.58	108.6	14.76	20.6	90.15
6	13.36	28.2	235.2	12.32	28.25	135.1	14.92	20.2	108.9
7	13.51	28.1	275.4	12.54	29.8	163.4	14.92	19.34	129.6
8	14.89	30.1	325.15	12.58	28.47	188.9	14.84	19.42	155.05
9	-	-	-	12.65	26.48	222.9	18.31	19.33	180.4
10				12.99	26.1	254.1	17.76	1.988	202.1
11				13.32	27.03	283.4	16.5	19.34	228.4
12				13.54	26.81	313	15.55	19.81	251.9
13				-	-	-	15.47	19.89	275.4
14							15.71	19.34	298
15							15.79	18.86	315.8
16							16.26	19.57	336.5

Appendix B- Digital corrections for errors introduced by experimental setup

The experimental setup introduced several types of errors. Without corrections, these errors will degrade the performance of the PADC system. Most errors are due to timing skew of pulse times, both in the modulation and detection processes. The following lists these errors and their corrections.

1. Inter-channel timing skew during detection

The optical hybrids' output ports were connected to the balanced detectors using optical fibers. Due to different fiber lengths, the pulses arrived at the detectors at different times. This has no effect if this timing skews are smaller than pulse spacing, but completely destroys the signal if not. In order to solve this, the channels were shifted in time, canceling this offset.

2. Pulse amplitude arrival time error due to delay lines

The delay lines setup, used to increase the sampling pulse rate from 80MHz to 1.28GHz, introduced significant differences between pulse amplitudes and arrival time errors. In principle amplitude errors are insignificant, as phase modulation is used. In practice, they have some effect due to channel mismatches and different calibration required for each channel. Timing was calibrated to the resolution limit of the oscilloscope used- approximately 25ps. For modulation frequencies higher than 1GHz, this corresponds to a significant phase error (up to 2 radians for 13GHz that was measured). Both of these errors were corrected using the following methodology:

- All channels are detected, and the amplitude of each modulated pulse is determined. This provides an $N \times M$ data matrix, where N is the number of balanced detectors and M the number of recorded pulses.
- The data matrix is separated according to pulse path, creating 16 $N \times (M/16)$ data matrices, where $16=2^4$ is the number of optical paths of the delay lines. These data sets are considered as individual sub-channels.
- Calibration parameters and timing offset is found for each sub-channel separately, and the phase is estimated for each one.
- The 16 phase data streams are treated as sub-ADCs in a time-interleaved architecture. They are merged together, and phase errors are corrected.

In a functional system, where the input signal is arbitrary and unknown, these corrections must be computed in advance and calibrated into the system. In the experimental system, these

parameters change between measurements, and global calibration was impossible. Instead we use that the signal is known (a pure sine with controllable frequency).

The easiest case is a frequency that is an integer multiplication of the MLL's pulse rate. This means that each sub-channel sees a constant phase value. Correcting for phase errors in this case simply amounts to adding a constant to each channel.

A much harder case is that of an arbitrary frequency. In this case, each sub-channel sees a sine wave- all with the same frequencies but different amplitudes, offsets and phases. These parameters must be equalized, and the phase offsets must be corrected to provide the proper timing difference between all channels.

The method used to accomplish this was fitting each sub-channel to a sine wave with the correct parameters, and then correcting each of the parameters to match the fit.